

Universidade de São Paulo  
Instituto de Física

# Vínculos Cosmológicos com o Auxílio do Efeito Sachs-Wolfe Integrado

Arthur Diniz Meirelles

Orientador: Prof. Dr. Edivaldo Moura Santos  
Coorientador: Prof. Dr. Ronaldo Carlotto Batista

Dissertação de mestrado apresentada ao Instituto de Física da Universidade de São Paulo, como requisito parcial para a obtenção do título de Mestre(a) em Ciências.

Banca Examinadora:

Prof(a). Dr. Edivaldo Moura Santos - Orientador (IF-USP)  
Prof(a). Dr(a). Nome do(a) Professor(a) (instituição de trabalho)  
Prof(a). Dr(a). Nome do(a) Professor(a) (instituição de trabalho)

São Paulo  
2024

FICHA DA BIBLIOTECA

University of São Paulo  
Physics Institute

# Cosmological Constraints using the Sachs-Wolfe Integrated Effect

Arthur Diniz Meirelles

Supervisor: Prof. Dr. Edivaldo Moura Santos  
Co-supervisor: Prof. Dr. Ronaldo Carlotto Batista

Dissertation submitted to the Physics Institute of the  
University of São Paulo in partial fulfillment of the  
requirements for the degree of Master of Science.

Examining Committee:

Prof. Dr. Edivaldo Moura Santos - Supervisor (IF-USP)  
Prof. Dr. Name (institution)  
Prof. Dr. Name (institution)

São Paulo  
2024

*Frase bonita*

# Agradecimentos

Este projeto, assim como qualquer outra conquista minha, não foi um trabalho individual, e sim a contribuição de um grande número de pessoas que me ajudaram, tiveram um impacto na minha vida e me influenciaram e motivaram de diversas formas diferentes, e essas influências têm tanta importância, se não mais, quanto apoios acadêmicos e financeiros. Frente à impossibilidade de dar os créditos a todos os contribuintes, tentarei me limitar aos principais.

Certamente os mais importantes são os membros da minha família, da qual todos contribuíram de alguma forma, mas eu tenho a obrigação de destacar meus pais, que lutaram contra várias adversidades para que eu chegassem onde eu cheguei, que me ensinaram o que é certo e como me dedicar, que não deixaram nada faltar a mim, e que até hoje seguem me motivando de formas diferentes, esses dois anos de muito trabalho e cansaço me fizeram ter muito mais admiração pelo esforço de ambos. Destaco ainda meus avós e minha tia Daniele, que tiveram imensa influência em quem eu sou, e contribuiram muito para a minha criação, e não posso deixar de agradecer aos meus vizinhos, Luis e Neuza, que podem não compartilhar do meu DNA, mas ajudaram a me criar como se eu fosse seus filhos, e eu tenho um imenso amor e gratidão por ambos.

Não posso deixar também de agradecer ao professor Edivaldo, que inspira a mim e a todos os seus orientandos com sua incrível competência, conhecimento, dedicação e paciência, eu acredito que esse projeto me ensinou muito além de cosmologia, e boa parte disso é graças ao senhor. Agradeço também ao professor Ronaldo, que complementou muito bem o projeto com ótimas ideias e discussões.

Outra parcela significativa dos créditos desse trabalho pertence à minha incrível namorada Carol, que está ao meu lado desde os anos em que eu era um aluno de graduação, e até antes como uma amiga muito importante, me apoiando, me inspirando e tornando meus dias melhores, mesmo que ela não perceba a influência que tem em tudo que eu faço e em quem eu sou, sobre o qual eu precisaria de muitas páginas para explicar.

Aos meus amigos, divido meus agradecimentos em duas partes: Aos que não estão envolvidos com física, pelo apoio emocional e companheirismo, pelas boas influências e motivações, e pelos bons momentos, que não deixam de contribuir para os meus esforços, deixo aqui um agradecimento especial a Pedro Augusto, que está comigo desde minha infância e até hoje tem

---

uma grande influência na minha vida, e me presta muito apoio; e aos meus amigos que estão envolvidos com a física, não só pelos motivos citados antes, mas também por muitos momentos e discussões construtivas, pelos grupos de estudo e pelas ajudas diretas em questões acadêmicas, destaco aqui meu amigo Leonardo Lessa, que me inspirou muito durante a graduação e me inspira até hoje a estudar cada vez mais para alcançar o potencial que eu sei que tenho mas ainda não alcancei.

O presente trabalho foi realizado com apoio do CNPq, Conselho Nacional de Desenvolvimento Científico e Tecnológico - Brasil.

# Abstract

ABSTRACT AQUI

**Keywords:**

# Resumo

[RESUMO AQUI](#)

**Palavras-chave:**

# List of Figures

1.1	Each image represents the same 10 square degree patch of the sky measured by the three telescopes shown above each image, the improvement in the resolution of each map is very noticeable. Credit: NASA/LAMBDA Science Team. . . . .	2
1.2	Illustration of the Integrated Sachs-Wolfe Effect, in which a photon is shown entering a deep gravitational well that flattens with time, leaving the photon with a net blueshift. Credit: DSSU Research. . . . .	2
2.1	A representation of the time evolution of the Universe, starting from the left (the Big Bang) with time passing towards the right. The radius of each section indicates the size of the Universe at that time; during inflation this radius increases very rapidly, indicating an accelerated expansion during this period, while closer to the present the slope of increase in size shows a slight acceleration, indicating the current dark energy accelerated period. Briefly after the inflation period (in cosmological time), the photons decouple from baryons, leaving a radiation field in the Universe, resulting in the CMB, represented in the image by the afterglow of inflation. After this, the only radiation in the Universe is this afterglow for many years, during that time structure starts to form from the small inhomogeneities left by quantum fluctuations in the very early stages of the Universe, forming the first stars and then the first galaxies. Credit: NASA/WMAP Science Team. . . . .	12
2.2	Planck 2018 CMB temperature power spectrum: the blue line corresponds to a $\Lambda$ CDM cosmology best-fit to the data points in orange. For $\ell < 30$ a logarithmic scale was used and the data points correspond to the $D_\ell^{TT}$ for each value of $\ell$ , while for $\ell \geq 30$ a linear scale was used and the data points correspond to binned values for the data for $D_\ell^{TT}$ . The error bars show $\pm 1\sigma$ uncertainties, including cosmic variance. Extracted from [6]. . . . .	19
2.3	Matter power spectrum calculated as a function of $k/h$ , where $h$ is the already defined reduced Hubble constant, using both a linear approximation and the so-called HALOFIT model[52] with cosmological parameters according to our fiducial $\Lambda$ CDM model. . . . .	22
2.4	CMB autocorrelation comparison for the late-ISW term and the full spectrum. Calculations were made using CAMB (for the full spectrum) and codes developed during the project. The parameters used are those corresponding to the Planck best fit parameters[6]. . . . .	24
2.5	Galaxy autocorrelation spectrum (left) and late-ISW contribution to the galaxy-CMB cross-correlation (right). The selection function used to calculate these spectra was parametrized to be compatible with 2MASS' galaxy redshift distribution[24, 49]. . . . .	25

## LIST OF FIGURES

---

2.6	The solid lines in the plots correspond to theoretical predictions for the CMB temperature autocorrelation spectra corresponding to different parameter values of the dark energy equation of state with $w_0 = -1$ , the black data points correspond to Planck's data[6]. Figures 2.6a, 2.6b and 2.6c show how the spectrum changes for a constant value of $w_a$ shown on the top left of the axis and varying speeds of sound, while the other three figures show how the curve behaves with varying values of $w_a$ and a constant speed of sound. All theoretical calculations were done using CAMB.	27
3.1	Selection function calculated for the 4 bands of the 2MASS catalog according to equation (3.1).	30
3.2	Selection function calculated for various parameter values according to the parametrization (3.1). Each plot is made by keeping 2 of its three parameters fixed, corresponding to the band 2 of the 2MASS catalog (see Table 3.1), the corresponding values of the varied parameter can be seen on the legend.	31
3.3	Mollweide projection of two instances of maps synthesized using HEALPix with the procedure presented.	32
3.4	Comparison between theoretical auto and cross-correlation spectra and the averages of the $C_\ell$ calculated from $10^4$ synthesized maps using the procedure presented in this section.	32
3.5	Distribution of cross-correlation values on different multipoles for $10^4$ maps synthesized with null cross-correlation. Gaussian fits of the samples are shown alongside the normalized distributions. As expected, the averages of the distributions are close to zero, and the variance of the distribution is significantly higher in low multipoles due to cosmic variance.	33
3.6	For each plot, one parameter is fixed at a certain value. The color of the plot indicates the ratio $P_{\text{null}}(z_0, \beta, \lambda) / P_{\text{null}}^{\text{2MASS}}$ , according to the bar on the right. Dark blue regions indicate the lower values of this ratio, these are the regions that improve the signal according to our analysis, and can indicate regions where a minimum value can be found. The constant values are: $\lambda = 5$ (upper left), $\beta = 1$ (lower left) and $z_0 = 0.17$ (lower right).	34
3.7	Comparison between theoretical properties of the point in parameter space that minimizes the null hypothesis and the band 1 of 2MASS.	35
4.1	Beam pattern for the Planck instrument at 30 GHz. Contours delineate the regions where the beam function drops from its maximum to 50%, 10%, 1% and 0.1% respectively. Source: Planck wiki.	38
4.2	Mollweide projection of the 3 WMAP9 CMB temperature maps with the combined 2MASS+WMAP mask applied.	41
4.3	Mollweide projection of the 2MASS-XSC galaxy contrast maps with the combined 2MASS+WMAP mask applied.	43
4.4	Comparison of theoretical correlation spectra for each band of the 2MASS catalog and the estimated correlation values using the method presented in the current chapter. Data points with error bars are the weighted average for channels Q, V, and W, with weights given by the reciprocal of noise variances. The red band corresponds to the cosmic variance, calculated using equations (4.17) and (4.18).	44

## LIST OF FIGURES

---

5.1	Joint posterior distributions of cosmological parameters using Planck's CMB temperature (T) and polarization (E) data. The TTTEEE dataset combines both autocorrelation data (TT and EE) and the cross-correlation data (TE). . . . .	47
5.2	Normalized $C^{tg}$ likelihood of each band of the 2MASS catalog and combination of all bands' likelihoods. The Planck best-fit for $\Omega_m$ is shown for comparison, the gray band represents represents the 68% error. . . . .	48
5.3	Normalized $C^{tg} + C^{gg}$ joint-likelihoods for each band of the 2MASS catalog and full joint-likelihood of all bands. The Planck best-fit for $\Omega_m$ is shown for comparison, the gray band represents represents the 68% error. . . . .	49
5.4	Normalized $C^{tg}$ likelihood calculated using synthetic data estimated as the theoretical cross-correlation obtained using the idealized band estimated in Chapter 3 for the selection function, with 2MASS' band 4 errors. The Planck best-fit for $\Omega_m$ is shown for comparison, the gray band represents represents the 68% error. . . . .	50

# List of Tables

2.1	Equation of state parameters $w$ , energy density functions $\rho(a)$ and energy density fractions for each known component of the Universe according to the $\Lambda$ CDM model. Most data were adapted from Planck[6], the radiation data was calculated based on [38]. . . . .	10
2.2	Best fit values of cosmological parameters reported by the Planck collaboration using a combined likelihood with temperature and polarization spectra and lensing data. Here $h = H_0/(100 \text{ km/s/Mpc})$ is the reduced Hubble constant, $\Theta_{MC}$ is the angular scale of the sound horizon at the surface of last scattering, $A_s$ is the amplitude of the primordial scalar perturbations, $n_s$ is the spectral index of the primordial scale perturbations, $\Omega_m = \Omega_c + \Omega_b$ is the matter energy density and $\sigma_8$ measures the amplitude of density fluctuations at the scale of $8h^{-1} \text{ Mpc}$ . The first 4 parameters, alongside are used for solving the perturbation equations with CAMB and the last 3 are derived from the solution. . . . .	20
2.3	Marginalized values and 68% confidence limits for cosmological parameters, assuming parametrization (2.57), obtained by combining Planck temperature and polarization autocorrelation and cross-correlation spectra[60], type IA supernovae data from the Joint Light Curve Analysis (JLA)[61] and BAO data from the Sloan Digital Sky Survey (SDSS)[62]. The $\Delta\chi^2$ value was computed with respect to the $\Lambda$ CDM best fits computed from the same data set combination. . . . .	26
3.1	Parameter values for the 4 bands of the 2MASS catalog. Values extracted from [49]. . . . .	29

# Contents

<b>1</b>	<b>Introduction</b>	<b>1</b>
<b>2</b>	<b>Cosmology's Concordance Model</b>	<b>5</b>
2.1	The Homogeneous Background . . . . .	5
2.1.1	Fundamental Observations and Principles . . . . .	5
2.1.2	Friedmann Equations . . . . .	6
2.1.3	Energy Content . . . . .	8
2.1.4	A Brief History of the Universe . . . . .	11
2.2	Inhomogeneities and Anisotropies . . . . .	12
2.2.1	Perturbed Space-Time . . . . .	13
2.2.2	The Boltzmann Equation . . . . .	14
2.3	The Cosmic Microwave Background . . . . .	17
2.3.1	CMB Autocorrelation Spectrum . . . . .	17
2.3.2	Analytical Approximation . . . . .	20
2.4	The Integrated Sachs Wolfe Effect . . . . .	21
2.4.1	The Matter Power Spectrum . . . . .	22
2.4.2	The Galaxy-CMB Correlation Spectra . . . . .	23
2.5	Dependence on Dark Energy Models . . . . .	25
<b>3</b>	<b>Optimizing the Selection Function</b>	<b>29</b>
3.1	Parametrization of the Selection Function . . . . .	29
3.2	Maximizing the Cross-Correlation Signal . . . . .	31
<b>4</b>	<b>Extracting Correlations from Data</b>	<b>36</b>
4.1	Two Point Functions . . . . .	36
4.2	Gibbs Sampling . . . . .	38
4.3	Data Sets and Analysis . . . . .	40
4.3.1	WMAP Data . . . . .	40
4.3.2	2MASS Catalog . . . . .	41
4.4	Correlation Spectra Obtained . . . . .	42
<b>5</b>	<b>Cosmological Constraints</b>	<b>45</b>
5.1	Monte Carlo Markov Chains . . . . .	45
5.2	Likelihoods . . . . .	47
5.3	MCMC Convergence . . . . .	51
<b>6</b>	<b>Conclusions</b>	<b>52</b>
<b>A</b>	<b>Demonstration of Accelerated Expansion Redshift</b>	<b>56</b>
<b>B</b>	<b>Demonstration of Correlation Functions</b>	<b>58</b>

# 1 | Introduction

The discovery of the Cosmic Microwave Background (CMB) is a fine example of serendipity, Arno A. Penzias and Robert W. Wilson found an unexpected excess temperature while measuring the effective zenith noise temperature in 1964, and after some investigation, they attributed this excess temperature to an isotropic radiation field that today we call the CMB [1]. The CMB has since been used as one of the main probes to studying cosmology, being able to provide various tests and insights into cosmological models [2–4] and measurements of cosmological parameters [5, 6].

In the concordance cosmological model, commonly called the  $\Lambda$ CDM model, the Universe was very compact and energetic at its very early stages, and has always been in expansion, resulting in a constant reduction in overall energy density. Eventually, when it reached temperatures of around 4000 K, photons decoupled from electrons and protons, which resulted in a radiation field that permeates the Universe ever since. This is, according to the  $\Lambda$ CDM model, the CMB[7]. The current measurement for the black body spectrum temperature of the CMB is 2.725 48(57) K [8], and despite being isotropic to many orders of precision, it does contain anisotropies in the order of  $10^{-5}$  K, which is expected in the  $\Lambda$ CDM model [9]. These fluctuations are the result of many physical effects that contribute to the CMB’s emission or are acting on the photons as they travel through the Universe, making them an excellent probe to constrain cosmological parameters.

Some mappings of the CMB were carried out in the last few decades, the first satellite launched specifically dedicated to doing this was the Cosmic Background Explorer (COBE) satellite with a  $7^\circ$  angular resolution [10], followed by the Wilkinson Microwave Anisotropy Probe (WMAP) with a  $0.3^\circ$  angular resolution, which was also able to show that CMB photons are polarized, a property related to other physical effects that assisted cosmologists in further understanding the history of the Universe[11–13]. In 2009, the Planck Satellite was launched, improving upon WMAP’s precision to an impressive value of  $5'$  ( $\sim 0.083^\circ$ ) angular resolution [14], allowing cosmologists to access the finest details in the CMB anisotropies to this day. Figure 1.1 shows a comparison between the resolution of these maps.

Amongst the many effects that affect the CMB, the Integrated Sachs-Wolfe (ISW) Effect is one of the most important ones. First described by Rainer K. Sachs and Arthur M. Wolfe in 1967,

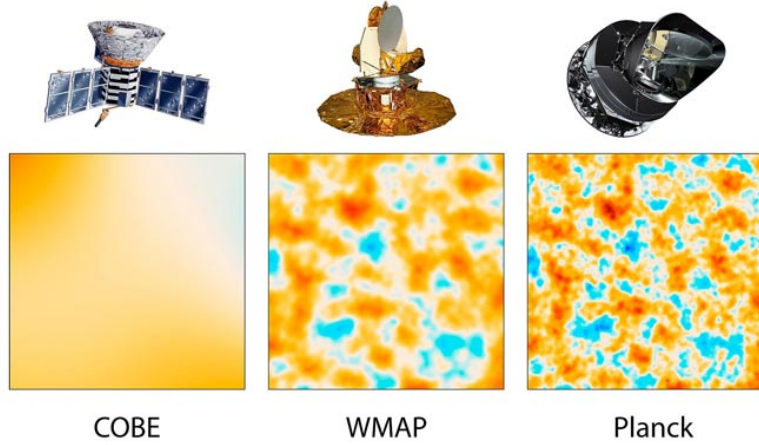


Figure 1.1: Each image represents the same 10 square degree patch of the sky measured by the three telescopes shown above each image, the improvement in the resolution of each map is very noticeable. Credit: NASA/LAMBDA Science Team.

the ISW effect is a mechanism that causes photons (including CMB photons) to blueshift or redshift in cosmological periods when gravitational potentials change rapidly. One such period is the time between the current dark energy dominated era and the dark matter dominated era before it. During this transition, gravitational potentials decay (or "flatten") over time, causing CMB photons that entered potential wells with a certain gravitational blueshift to leave these wells with a redshift that does not compensate for the initial blueshift, leaving a net blueshift in these photons, creating patterns that can be observed in the CMB temperature map and spectrum[15].

This mechanism is illustrated in Figure 1.2.

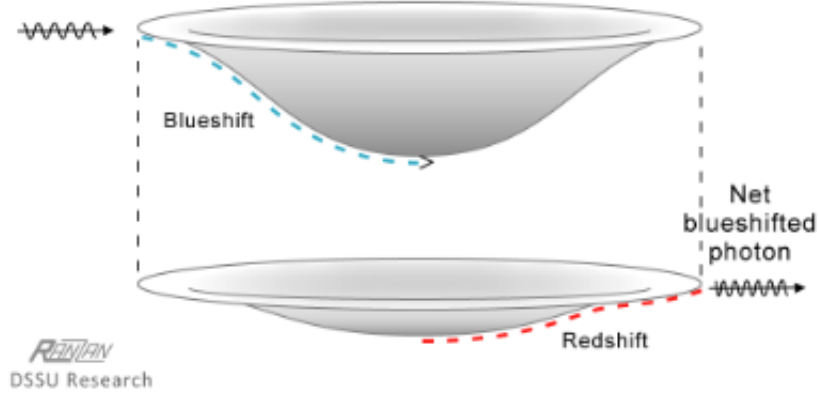


Figure 1.2: Illustration of the Integrated Sachs-Wolfe Effect, in which a photon is shown entering a deep gravitational well that flattens with time, leaving the photon with a net blueshift. Credit: DSSU Research.

There are two contributions to the ISW effect: The early-time ISW effect occurs immediately after the last scattering surface, and the late-time ISW effect, which is more recent, occurring in the transition to the current dark energy dominated era.

From this association between blueshifted CMB photons and gravity wells, it is natural to assume that the matter distribution of the Universe should hold a statistical cross-correlation with the CMB temperature map. When looking at the theoretical model, we will see that this cross-correlation is expected[16, 17], and many works in the past have reported detections of the ISW effect using such cross-correlation using various sources of data and statistical methods[18–21]. Overall, the ISW signal was favored in these works, but mostly with low significance levels. We highlight the results shown in [22], in which many large scale structure tracers were combined to obtain a  $4\sigma$  detection, from which the two main contributors were Planck’s convergence lensing maps (Kappa) and the NRAO VLA Sky Survey (NVSS)[23].

The present work uses the bayesian methods presented in [24] to estimate these cross-correlation spectra using CMB temperature maps from WMAP[5, 25] and galaxy contrast maps provided by the Two Micron All Sky Survey (2MASS)[26], and study the constraint power of the results over a specific cosmological parameter. We have also investigated the impact of the redshift distribution of the galaxies in the catalog used on the resulting cross-correlation spectrum, and studied what would be the distribution that optimizes this signal.

The rest of this dissertation will be organized as follows:

In Chapter 2, we start by presenting the fundamental observations and principles of cosmology, some of its fundamental equations, and discuss what makes up the  $\Lambda$ CDM model. We first describe the universe in terms of a homogeneous and isotropic background and later introduce perturbations to this background, which allows us to determine the linear differential equations that describe the energy contents of the universe. With these equations, we can focus on the radiation equation to describe the statistical distribution of the CMB today, finally reaching a point where we can mathematically define the ISW effect and its properties, as well as discuss the so called cosmic variance, a source of irreducible error in the signal. Finally, we discuss how alternative dark energy models can influence our observables.

In Chapter 3, we study how the redshift distribution of galaxy catalogs are generally parametrized, the general properties of this parametrization and the distributions of the 4 bands we are using of the 2MASS catalog. In order to maximize the cross-correlation signal taking

into account the high cosmic variance in this region, we define the probability that a certain cross-correlation function calculated from a certain galaxy distribution is compatible with a 0 cross-correlation model and determine the parametrization that minimizes this probability.

In Chapter 4, we briefly discuss some of the properties of the data obtained from the satellites and some traditional methods used to process that data, motivating the discussion about the Monte Carlo method used in this work. Later, the WMAP and 2MASS data are described, the final maps used are shown, as well as the results for the correlation spectra obtained from these maps, showing how present cosmic variance is in the region.

Finally, in Chapter 5, the method used to calculate the constraints on the cosmological parameter  $\Omega_m$  – which will be defined in Chapter 2 – for the correlation spectra is discussed. We have studied these constraints not only for the 4 2MASS bands, but also for an artificial dataset generated based on the idealized galaxy redshift distribution found in Chapter 3.

We summarize all the results from this project in Chapter 6, draw some conclusions based on this and other works that have studied the same problem in various different ways, and present future perspectives.

## 2 | Cosmology's Concordance Model

The advent of general relativity in the early 20th century allowed physicists to conceptualize mathematical models of the Universe. Albert Einstein proposed a model for a static Universe using his theory[27], and other Universe models were proposed in the following years. To start this chapter, the fundamental principles of cosmology will be discussed and used to setup a simple background for the Universe, and the specificities of the currently most accepted model for the Universe – the  $\Lambda$ CDM model – will be discussed. After this, we will complement this simple background with finer details and provide a statistical description of cosmological observables that can be used to test our models.

### 2.1 The Homogeneous Background

#### 2.1.1 Fundamental Observations and Principles

One of the fundamental principles of cosmology is called the Cosmological Principle: at large scales, the Universe is both homogeneous and isotropic. This principle can be used to simplify the description of the energy distribution in the Universe, but it also simplifies the possible metrics that can describe the Universe to those that have constant curvature (a quantity denoted as  $k$ ), and it can be shown that any space with constant curvature is locally isometric to: The Euclidian flat space ( $k = 0$ ), a hyperspherical space ( $k = +1$ ) or a hyperbolic space ( $k = -1$ )[28]. The Cosmological Principle has support from a good amount of cosmological observations, such as the CMB[10], the galaxy sky distribution[29, 30], amongst others.

In the period from 1927 to 1929, Edwin Hubble and Georges Lemaître, amongst other scientists, greatly contributed to the current understanding of cosmology: Observations were carried out and showed that most galaxies and nebulae data show a redshift proportional to their distances relative to the earth[31], these results were studied using general relativity and cosmological models at the time[32]. It was then established another principle that physicists were avoiding in their theoretical models for quite some time: The Universe is not static, in fact it is expanding, and for objects not too far, there is a linear relationship between the redshift of an observed object and its distance to the observer.

To describe the Universe, a coordinate system is embedded in the entire Universe, and to describe its dynamical nature, the scale factor  $a$  is introduced to the theoretical model:  $a$  is set to 1 at the present as a convention (usually called  $a_0$ ), and its value at any given time  $a(t)$  is the size of the Universe relative to its present size. A simple relation can be established between the scale factor of an observed object and its redshift  $z$ :

$$1 + z = \frac{\lambda_{\text{obs}}}{\lambda_{\text{emit}}} = \frac{a_{\text{obs}}}{a_{\text{emit}}} = \frac{1}{a_{\text{emit}}} \quad (2.1)$$

where  $\lambda$  and  $a$  are the wavelength of the radiation and the scale factor, respectively, when emitted ( $\lambda_{\text{emit}}$  and  $a_{\text{emit}}$ ) and when observed ( $\lambda_{\text{obs}}$  and  $a_{\text{obs}}$ ).

$$H(t) = \frac{1}{a} \frac{da}{dt} \quad (2.2)$$

These properties are not exclusive to a particular cosmological model, instead being present in all of them. The standard model of cosmology, called  $\Lambda$ CDM, usually takes a few assumptions on top of the ones described previously:

- During the very early stages of the Universe, it was very compact and energetic, and eventually it went through a period of rapidly accelerated expansion, called the inflation period, which was driven by a scalar quantum field;
- Aside from baryonic matter, radiation and neutrinos, there are two other main components in the Universe: non-relativistic (cold) dark matter and an energy component with constant density called dark energy, which is related to a cosmological constant  $\Lambda$ ;

Based on the Cosmological Principle, most theoretical models first set up a homogeneous and isotropic background description of the Universe, and then introduce perturbations to this background, allowing for a detailed statistical description of its evolution. In the rest of this section, we will use the principles and assumptions just presented to set this background.

### 2.1.2 Friedmann Equations

As already mentioned, the main theoretical framework to describe the Universe is the theory of general relativity, since the most relevant force in the scale of the Universe is the gravitational one. We then use Einstein's field equations with a cosmological constant  $\Lambda$ :

$$R_{\mu\nu} - \frac{1}{2}g_{\mu\nu}R + \Lambda g_{\mu\nu} = 8\pi G T_{\mu\nu}, \quad (2.3)$$

where  $R_{\mu\nu}$  is the Ricci curvature tensor for the Universe's metric  $g_{\mu\nu}$ ,  $R \equiv g_{\mu\nu}R^{\mu\nu}$  is the Ricci scalar,  $G$  is the gravitational constant and  $T_{\mu\nu}$  is the energy-momentum tensor.

In equation (2.3) and throughout this text (unless otherwise stated), we will use units such that the Boltzmann constant ( $k_b$ ), the speed of light in a vacuum ( $c$ ) and the reduced Planck constant ( $\hbar$ ) are all equal to one. Furthermore, Greek letter tensor indices indicate that the time component of the tensor is included in the equation and Latin letter tensor indices indicate that only spatial components are included. Current results strongly indicate the metric  $g_{\mu\nu}$  of the Universe to be flat ( $k = 0$ )[6], thus justifying the use of an Euclidian metric scaled by  $a(t)$ , and we will assume a homogeneous and isotropic distribution of energy throughout the Universe to construct an energy-momentum tensor with constant energy density  $\rho_0$  and constant pressure  $P$ [33]:

$$g_{\mu\nu} = \begin{pmatrix} -1 & 0 & 0 & 0 \\ 0 & a^2 & 0 & 0 \\ 0 & 0 & a^2 & 0 \\ 0 & 0 & 0 & a^2 \end{pmatrix} \quad T_{\mu\nu} = \begin{pmatrix} -\rho_0 & 0 & 0 & 0 \\ 0 & P & 0 & 0 \\ 0 & 0 & P & 0 \\ 0 & 0 & 0 & P \end{pmatrix}. \quad (2.4)$$

The metric  $g_{\mu\nu}$  described in equation (2.4) is called the Friedmann-Lemaître-Robertson-Walker (FLRW) metric[34]. In order to expand any equation from (2.3), it is necessary to determine  $R = g^{\mu\nu}R_{\mu\nu}$ . By expanding the expression using the matrices defined in (2.4), the result is

$$R = 6 \left[ \frac{\ddot{a}}{a} + \left( \frac{\dot{a}}{a} \right)^2 \right]. \quad (2.5)$$

From all the equations in (2.3), if the one corresponding to  $\mu = \nu = 0$  is expanded using the result (2.5), one obtains

$$\left( \frac{\dot{a}}{a} \right)^2 = \frac{1}{3} (8\pi G \rho_0 + \Lambda), \quad (2.6)$$

which relates the relative rate at which the Universe is expanding with the energy content of

the Universe. In the  $\Lambda$ CDM model,  $\Lambda$  is assumed to be the source of the current accelerated expansion of the Universe, so an energy component related to this constant is necessary, and its energy density can be defined as

$$\rho_\Lambda = \frac{\Lambda}{8\pi G}, \quad (2.7)$$

such that

$$\left(\frac{\dot{a}}{a}\right)^2 = \frac{8\pi G}{3}\rho, \quad (2.8)$$

where  $\rho = \rho_\Lambda + \rho_0$ . This is called Friedmann's first equation.

When any of the space-space equations of (2.3) is expanded and the resulting equation is combined with equation (2.8), Friedmann's second equation is obtained:

$$\frac{\ddot{a}}{a} = -\frac{4\pi G}{3}(\rho + 3P). \quad (2.9)$$

This equation is a relation between the acceleration of the Universe and its energy content. It is clear that  $P < -\frac{1}{3}\rho$  indicates a Universe expanding with a positive acceleration, which is highly unexpected since gravity is an attractive force, but in section 2.1.3 the case of the cosmological constant will be discussed, in which  $\Lambda$  yields  $P_\Lambda = -\rho_\Lambda$ , being the reason it contributes to an accelerated expansion.

### 2.1.3 Energy Content

To understand the contribution of each component of the Universe to its dynamics, a differential equation for each component has to be determined, we do this using the energy-momentum conservation equation:

$$\nabla_\mu T_\nu^\mu \equiv \partial_\mu T_\nu^\mu + \Gamma_{\alpha\mu}^\mu T_\nu^\alpha - \Gamma_{\nu\mu}^\alpha T_\alpha^\mu = 0. \quad (2.10)$$

Again using the energy-momentum tensor defined in (2.4), the following equation is obtained:

$$\frac{\partial\rho}{\partial t} + \frac{\dot{a}}{a}(3\rho + 3P) = 0. \quad (2.11)$$

To solve this, a relation between density and pressure for each component of the Universe is needed, an equation of state. It is commonly assumed that, for a given component  $s$  of the Universe, its equation of state takes the form

$$P_s = w_s \rho_s, \quad (2.12)$$

where  $w_s$  is called the equation of state parameter. Using that equation and solving for  $\rho_s(a)$  on equation (2.11) yields

$$\rho_s(a) \propto \exp \left[ -3 \int_1^a \frac{da'}{a'} [1 + w_s(a')] \right]. \quad (2.13)$$

This solution ignores further interaction between components, it would apply to a single-component Universe, but it is also a useful first approximation in epochs of dominance of a single component. In the  $\Lambda$ CDM model, it is assumed that all components of the Universe possess a constant value for  $w_s$ , in that case the solution is simple:

$$\rho_s(a) \propto a^{-3(1+w_s)}. \quad (2.14)$$

This represents the evolution of the density parameter of any component as a function of the scale parameter, and thus as a function of cosmological time, since  $a(t)$  is monotonically increasing (the Universe has not reduced at any point in its history so far).

The rigorous form of determining  $w_s$  for some components of the Universe requires the usage of statistical physics. In cases where we have limited information on the physical properties of a certain component, such as dark energy, theoretical frameworks and assumptions have to be used, as well as the analysis of data.

In the case of dark energy, assuming its origin is related to the cosmological constant, the data strongly suggests a value of  $w_\Lambda = -1$ , which also indicates a constant density for dark energy. From the quantum field theory point of view, the cosmological constant energy density would be associated to zero point energy of a quantum field. However, so far, no calculation has been successful in predicting a zero point energy whose density is consistent with the cosmological observations[35]. Many models propose alternative possibilities, such as dynamical dark energy in which  $w_{DE}$  is a function of  $a$ [36], which would still be able to explain the accelerated expansion of the Universe as long as  $w_{DE} < -\frac{1}{3}$ , these are discussed in more detail in section

2.5. Table 2.1 summarizes the equation of state properties of each known component in the Universe.

It is very useful to also define the energy density fraction of each component of the Universe using

$$\Omega_s = \frac{\rho_s(a_0)}{\rho_{\text{crit}}}, \quad (2.15)$$

where  $\rho_{\text{crit}}$  is the so called critical density, defined as

$$\rho_{\text{crit}} \equiv \frac{3H_0^2}{8\pi G} \approx 8.5 \times 10^{-27} \text{ kg/m}^3, \quad (2.16)$$

where  $H_0$  is the Hubble constant, the value of the Hubble parameter  $H(t)$  defined in (2.2) at the present.

This energy density makes it possible to determine what is the curvature of the Universe: if the total sum of energy densities in the Universe is equal to the critical density, the Universe is flat; if this sum is higher than  $\rho_{\text{crit}}$  the Universe would have positive curvature; and if this sum is lower than  $\rho_{\text{crit}}$ , the Universe would have negative curvature[37].

Table 2.1 summarizes the current estimated values for these energy fractions for the Universe in the present. It is important to note that commonly in cosmology (and throughout this text), the classification of baryons includes electrons, even though, according to the standard model of particle physics, electrons belong, together with their associated neutrinos, to one of the three families of leptons.

Component	$\rho(a)$	$w$	$\Omega$
Baryonic matter ( $\Omega_b$ )	$\rho_0 a^{-3}$	0	0.05
Cold dark matter ( $\Omega_c$ )	$\rho_0 a^{-3}$	0	0.26
Radiation ( $\Omega_r$ )	$\rho_0 a^{-4}$	$\frac{1}{3}$	$5.29 \times 10^{-5}$
Dark energy ( $\Omega_\Lambda$ )	$\rho_0$	-1	0.68
Curvature ( $\Omega_k$ )	$\rho_0 a^{-2}$	$-\frac{1}{3}$	0.001

Table 2.1: Equation of state parameters  $w$ , energy density functions  $\rho(a)$  and energy density fractions for each known component of the Universe according to the  $\Lambda$ CDM model. Most data were adapted from Planck[6], the radiation data was calculated based on [38].

### 2.1.4 A Brief History of the Universe

We commonly categorize different stages of the Universe according to important events that happened during its history. The  $\Lambda$ CDM model assumes the Universe started as a singularity; as it started expanding, quantum fluctuations at that time would eventually result in inhomogeneities thought to be the source for the formation of structures.

The next important period of the Universe's evolution was a highly accelerated expansion epoch driven by an effect called cosmic inflation, first proposed as a solution to the horizon problem[39, 40], related to how can the CMB temperature differences across the sky be so small ( $\sim 10^{-5}$  K), even between points apparently causally disconnected during all epochs of the Universe's thermal history. The  $\Lambda$ CDM model assumes inflation was driven by a quantum scalar field[33]. Definitive evidence of the inflationary model may be reached with the detection of a certain type of polarization of the CMB called the B-modes, which have not been detected yet, but have reached good constraints.[13]

Briefly after inflation, baryons and photons are still coupled through Compton scattering, thus photons are still unable to travel freely. The Universe at this point is composed of photons coupled with baryons, helium nuclei, and trace amounts of lithium. With the decrease in temperature, hydrogen atoms can form without being quickly ionized, Compton scattering eventually can no longer maintain baryons and photons coupled, resulting in a decoupling of these components. The photons are released to travel across the Universe, the radiation field formed from this period is what we currently measure as the CMB.

After this, an epoch called "the Dark Ages" starts, in which the photons in the Universe are the result of the decoupling described before and stars are yet to be formed, which is the reason why it is called a dark age. Matter dominates this period, greatly decreasing the rate of expansion of the Universe. As a result of the quantum fluctuations in the early Universe, stars, galaxies, and other structures form. The study of the formation of structure is completely dependent on the study of the inhomogeneities of the Universe at small scales, where the cosmological principle is no longer expected to be valid. Some details of this theoretical framework will be covered in the next section.

Figure 2.1 shows a summarized and visual representation of some of the events described in this section.

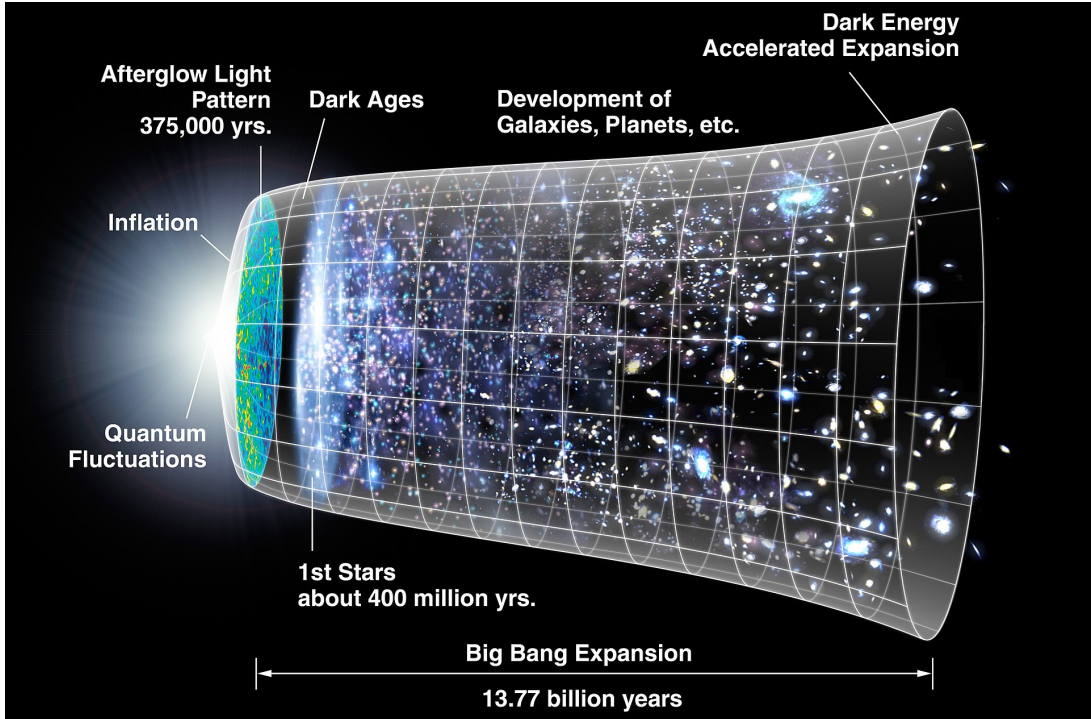


Figure 2.1: A representation of the time evolution of the Universe, starting from the left (the Big Bang) with time passing towards the right. The radius of each section indicates the size of the Universe at that time; during inflation this radius increases very rapidly, indicating an accelerated expansion during this period, while closer to the present the slope of increase in size shows a slight acceleration, indicating the current dark energy accelerated period. Briefly after the inflation period (in cosmological time), the photons decouple from baryons, leaving a radiation field in the Universe, resulting in the CMB, represented in the image by the afterglow of inflation. After this, the only radiation in the Universe is this afterglow for many years, during that time structure starts to form from the small inhomogeneities left by quantum fluctuations in the very early stages of the Universe, forming the first stars and then the first galaxies. Credit: NASA/WMAP Science Team.

## 2.2 Inhomogeneities and Anisotropies

The existence of structures – nebulae, stars, galaxies, clusters – in the Universe indicates that, throughout its history, it has been inhomogeneous and anisotropic at some scale. These perturbations to the uniform background are relatively small though, take the CMB for instance: CMB anisotropies are around 5 orders of magnitude lower than its average blackbody temperature[5].

In this scenario, there is no known theoretical model that can predict the exact behavior of every particle in the Universe. Therefore, we turn to a statistical prediction taking into account the properties of space-time and the components of the Universe. In this section, the first order equations that govern these properties will be shown by introducing perturbations both to the

metric and to the stress-energy tensor.

### 2.2.1 Perturbed Space-Time

In the  $\Lambda$ CDM model, to account for perturbations in the uniform background previously set, we use the following new form for the metric:

$$\begin{cases} g_{00} = -1 - 2\Psi(\mathbf{x}, t), \\ g_{0i} = g_{i0} = 0, \\ g_{ij} = a^2(t)\delta_{ij}[1 + 2\Phi(\mathbf{x}, t)]. \end{cases} \quad (2.17)$$

In equation (2.17),  $\Psi$  corresponds to the Newtonian potential and governs the movement of nonrelativistic objects[33], while  $\Phi$  is a perturbation to the spatial curvature.

With the use of the geodesic equation on this new tensor and using a first order approximation, it is possible to obtain the following results for the motion equations of particles traveling through the perturbed space-time:

$$\frac{dx^i}{dt} = \frac{\hat{p}_i}{a} \frac{p}{E} (1 - \Phi + \Psi), \quad (2.18)$$

$$\frac{dp^i}{dt} = -(H + \dot{\Phi})p^i - \frac{E}{a}\partial_i\Psi - \frac{1}{a}\frac{dp^i}{dE}p^k\partial_k\Phi + \frac{p^2}{aE}\partial_i\Phi. \quad (2.19)$$

We can use

$$\frac{dp}{dt} = \frac{d}{dt}\sqrt{\delta_{ij}p^i p^j} = \delta_{ij}\frac{p^i}{p}\frac{dp^j}{dt} \quad (2.20)$$

and  $\hat{p}^i = p^i/p$  in combination with equation (2.19) to find separate equations for  $p$  and  $\hat{p}^i$ :

$$\frac{dp}{dt} = -[H + \dot{\Phi}]p - \frac{E}{a}\hat{p}^i\partial_i\Psi, \quad (2.21)$$

$$\frac{d\hat{p}^i}{dt} = \frac{E}{ap}[\delta^{ik} - \hat{p}^i\hat{p}^k]\partial_k\left(\frac{p^2}{E^2}\Phi - \Psi\right). \quad (2.22)$$

As for the dynamics of the field perturbations, it is possible to use Einstein's field equations to obtain, in Fourier space, the equations for scalar perturbations on the gravitational potentials[33]

$$k^2\Phi + 3H(\dot{\Phi} - H\Psi) = -4\pi Ga^2(\rho_{DM}\delta_{DM} + \rho_b\delta_b + 4\rho_\gamma\Theta_0 + 4\rho_\nu\mathcal{N}_0), \quad (2.23)$$

$$k^2(\Phi + \Psi) = -32\pi Ga^2(\rho_\gamma\Theta_2 + \rho_\nu\mathcal{N}_2). \quad (2.24)$$

Here,  $\rho$  indicates the average density of a component,  $\delta$  represents the perturbation to these densities, and the indexes  $DM$ ,  $b$ ,  $\gamma$  and  $\nu$  indicate the quantities related to dark matter, baryons, radiation and neutrinos respectively. The terms  $\Theta_0$ ,  $\Theta_2$ ,  $\mathcal{N}_0$  and  $\mathcal{N}_2$  are obtained in the calculation of the perturbed energy-momentum tensor, they are defined as

$$F_\ell = \frac{1}{(-i)^\ell} \int_{-1}^1 \frac{\mathcal{P}_\ell(\mu)F(\mu)}{2} d\mu, \quad (2.25)$$

where  $F$  can either represent  $\Theta$  or  $\mathcal{N}$ ;  $\mu = \hat{k} \cdot \hat{p}$  is the cosine between the momentum direction of the photon and the Fourier space wavevector;  $P_\ell$  are Legendre polynomials; the functions  $\Theta(\mu)$  and  $\mathcal{N}(\mu)$  are dimensionless fields that quantify the perturbations of photon and neutrino distributions with respect to the homogeneous background; and  $i$  is the imaginary unit  $i^2 = -1$ .

### 2.2.2 The Boltzmann Equation

The Boltzmann equation is a fundamental component in the study of every component of the Universe. One general form of writing the Boltzmann equation is

$$\frac{df}{dt} = \frac{\partial f}{\partial t} + \frac{\partial f}{\partial x^i} \cdot \frac{dx^i}{dt} + \frac{\partial f}{\partial p} \frac{dp}{dt} + \frac{\partial f}{\partial \hat{p}^i} \cdot \frac{d\hat{p}^i}{dt} = C[f], \quad (2.26)$$

where  $f$  is the distribution function of the component to be analyzed and  $C[f]$  is the collision term, a factor that is calculated by considering the interactions of such components.

Using equations (2.21) and (2.22) with the Boltzmann equation and assuming  $E = p$ , i.e. assuming a relativistic particle such as photons, the full first order Boltzmann equation for photons is

$$\begin{aligned} \frac{df}{dt} = & \frac{\partial f}{\partial t} + \frac{\partial f}{\partial x^i} \frac{\hat{p}^i}{a} (1 - \Phi - \Psi) - \frac{\partial f}{\partial p} \left\{ [H + \dot{\Phi}]p + \frac{1}{a} p^i \partial_i \Psi \right\} \\ & + \frac{\partial f}{\partial \hat{p}^i} \frac{1}{a} \left[ \partial_i (\Phi - \Psi) - \hat{p}^i \hat{\partial}^k \partial_k (\Phi - \Psi) \right]. \end{aligned} \quad (2.27)$$

The first order approximation is being used, and so it is possible to simplify this expression

further. For instance, the distribution  $f$  for the homogeneous background takes the form of Bose-Einstein's distribution, which means there is no dependence on  $\hat{p}^i$  and  $x^i$  in this case. It is commonly assumed that the deviations from this distribution are of the same order of the perturbations  $\Phi$  and  $\Psi$ , so both  $\frac{\partial f}{\partial x^i}$  and  $\frac{\partial f}{\partial \hat{p}^i}$  are first order factors, multiplied by  $\Phi$  or  $\Psi$  result in second order terms which can be neglected, resulting in

$$\frac{df}{dt} = \frac{\partial f}{\partial t} + \frac{\hat{p}^i}{a} \frac{\partial f}{\partial x^i} - \left[ H + \dot{\Phi} + \frac{1}{a} \hat{p}^i \partial_i \Psi \right] p \frac{\partial f}{\partial p}. \quad (2.28)$$

This is an important equation for the description of the CMB, but the description of anisotropies for massive particles is still important, for which the same assumptions are made, resulting in

$$\frac{df}{dt} = \frac{\partial f}{\partial t} + \frac{p}{Ea} \hat{p}^i \frac{\partial f}{\partial x^i} - \left[ H + \dot{\Phi} + \frac{E}{ap} \hat{p}^i \partial_i \Psi \right] p \frac{\partial f}{\partial p}. \quad (2.29)$$

The only difference between these equations is the term  $E/p$  which, in the case of radiation, is equal to 1. The first order approximation for non-relativistic matter breaks down in the late Universe, a non-linear model is necessary in this scenario.

To arrive at a differential equation, a function to describe the perturbations needs to be defined, and so does the distribution function. Taking the CMB as an example, the perturbed form of the temperature distribution for CMB photons in general can be defined as

$$T(\mathbf{x}, \hat{\mathbf{p}}, t) = \bar{T}(t)[1 + \Theta(\mathbf{x}, \hat{\mathbf{p}}, t)], \quad (2.30)$$

where  $\bar{T}$  is the average temperature in a given time and  $\Theta$  is the same field presented in equation (2.25), that quantifies the perturbations of the CMB distribution with respect to its average value. This perturbation field can be expressed in terms of the set of functions  $\Theta_\ell$  defined in (2.25) by the following equation in Fourier space:

$$\Theta(\hat{\mathbf{k}}, \mu) = \sum_{\ell=0}^{\infty} (2\ell + 1)(-i)^\ell \Theta_\ell(\hat{\mathbf{k}}) \mathcal{P}_\ell(\mu). \quad (2.31)$$

If we use the Bose-Einstein distribution for the temperature defined in (2.30) and expand it to its first order, we obtain

$$f(\mathbf{x}, \mathbf{p}, t) = f^{(0)}(p, t) - p \frac{\partial f^{(0)}(p, t)}{\partial p} \Theta(\mathbf{x}, \mathbf{p}, t), \quad (2.32)$$

where

$$f^{(0)}(p, t) = \left[ \exp\left(\frac{p}{T}\right) - 1 \right]^{-1} \quad (2.33)$$

We can then expand the Boltzmann equation using the results in (2.32) and (2.33) and take into account Compton scattering to calculate the collision term  $C[f]$  to obtain a differential equation for the CMB photons. We can use similar procedures, using adequate distribution functions, and obtain a set of coupled differential equations to describe the evolution of the perturbations of every known component of the Universe in Fourier space[33]:

$$\dot{\Theta} + \frac{ik\mu}{a}(\Theta + \Psi) = -\dot{\Phi} - \dot{\tau} \left[ \Theta_0 - \Theta + \mu v_b - \frac{1}{2} \mathcal{P}_2(\mu)(\Theta_2 + \Theta_{P2} + \Theta_{P0}) \right], \quad (2.34)$$

$$\dot{\delta}_c + \frac{ik}{a}v_c = -3\dot{\Phi}, \quad (2.35)$$

$$\dot{\delta}_b + \frac{ik}{a}v_b = -3\dot{\Phi}, \quad (2.36)$$

$$\dot{v}_c + \frac{H}{a}v_c = -\frac{ik}{a}\Psi, \quad (2.37)$$

$$\dot{v}_b + \frac{H}{a}v_b = -\frac{ik}{a}\Psi + \frac{4\rho_\gamma}{3\rho_b}\dot{\tau}(v_b + 3i\Theta_1), \quad (2.38)$$

$$\dot{\mathcal{N}} + \frac{ik\mu}{a}\mathcal{N} = -\dot{\Phi} - \frac{ik\mu}{a}\Psi. \quad (2.39)$$

Here,  $\Theta_{P\ell}$  is defined by equation (2.25) using  $F = \Theta_P$ , where  $\Theta_P$  is the polarization field;  $\delta$  and  $\delta_b$  are the perturbations to the matter and baryon distributions respectively;  $v$  and  $v_b$  are the bulk velocities of the fluids in the stress-energy tensor for matter and baryons respectively;  $\rho_b$  and  $\rho_\gamma$  are the baryon and radiation energy densities respectively; and  $\tau$  is the optical depth to recombination, which in this context measures the transperancy of the Universe at a certain redshift  $z$ :

$$\tau(z) = \int_0^z \frac{\sigma_T n_e(z')}{H(z')} dz', \quad (2.40)$$

where  $\sigma_T$  is the Thomson scattering cross-section and  $n_e$  is the number density of free electrons in the Universe at redshift  $z'$ .

These equations, alongside equations (2.23) and (2.24), are very complex to be solved analytically, so it is common to evolve them numerically, and there are a few codes developed specifically to do this. One of them, that has been used in this project, is CAMB.[41, 42]

## 2.3 The Cosmic Microwave Background

With the dynamical equations for photons determined, one can obtain the temperature perturbation distribution  $\Theta$  if initial conditions are provided. With the equations already presented, it is possible to show that the initial conditions at the early Universe depend only on the initial conditions for  $\Phi$ [33], which are then evolved through the inflationary period assuming the existence of a quantum scalar field  $\phi(\mathbf{x}, t)$  that drives a brief accelerated expansion.

With time, particles start to form: Quarks, hadrons, neutrinos, amongst others, at different times. Eventually baryons have formed and the photons are tightly coupled to them, forming a baryon-photon fluid that can be described by the differential equations (2.34) - (2.39), the initial distribution obtained for this fluid can then be used as the initial condition and evolved to predict the present anisotropies to the uniform background. To analyze these predictions, the statistical behavior of each component of the Universe is taken: either their spectral densities – usually called their power spectra – or what is known as their correlation spectra.

### 2.3.1 CMB Autocorrelation Spectrum

Equation (2.30) explicitly assumes a dependence in position, time, and momentum direction. Measurements made on Earth can assume a fixed value for time since our measurements related to the Universe are taken in a period negligible in the cosmological scale, but the translational movement of the Earth is relevant to our measurements: measurements of the CMB made by a non-comoving observer, when projected onto a sphere, lead to a strong dipole pattern in the temperature distribution, modulation of the multipole terms and a small relativistic aberration at angular scales of a few arcminutes[43–45].

Despite these effects, measurements of the temperature distribution can be projected onto a sphere independent of the Earth’s position, making it possible to describe this distribution simply

using two angle variables, or simply  $\hat{\mathbf{p}}$ .

We can expand the temperature perturbations in spherical harmonics:

$$\Theta(\mathbf{x}, \hat{\mathbf{p}}, t) = \sum_{\ell=1}^{\infty} \sum_{m=-\ell}^{\ell} a_{\ell m}(\mathbf{x}, t) Y_{\ell m}(\hat{\mathbf{p}}). \quad (2.41)$$

All the information about temperature maps of the CMB measured on Earth are contained in the set of  $a_{\ell m}$  values. Given the limited number of pixels  $N_{\text{pix}}$  of any of these maps, there is a maximum value of  $\ell$  ( $\ell_{\max}$ ) up to which statistically meaningful information can be retrieved. For each value of  $\ell$ , there are  $2\ell + 1$  values of  $m$  – and  $a_{\ell m}$  – in the series, a hypothetical observed map with precision  $p_r$  in squared radians would have  $4\pi/p_r$  pixels, setting this number of pixels equal to the number of  $a_{\ell m}$  used to describe this map gives a reasonable estimation of  $\ell_{\max}$ [33], so

$$\sum_{\ell=0}^{\ell=\ell_{\max}} (2\ell + 1) = (\ell_{\max} + 1)^2 = N_{\text{pix}} = \frac{4\pi}{p_r}. \quad (2.42)$$

Using the orthogonality property of the spherical harmonics, one can obtain a direct expression for  $a_{\ell m}$  in terms of the angular distribution of the perturbations:

$$a_{\ell m}(\mathbf{x}, t) = \int \frac{d^3 k}{(2\pi)^3} e^{i\mathbf{k}\cdot\mathbf{x}} \int d\Omega Y_{\ell m}^*(\hat{\mathbf{p}}) \Theta(\mathbf{k}, \hat{\mathbf{p}}, t). \quad (2.43)$$

Again, there are available codes that efficiently and precisely calculate  $a_{\ell m}$  from a pixelized map and vice versa, the one used in this work was HEALPix[46]. Under the hypothesis that the spherical harmonics coefficients  $a_{\ell m}$  are independent Gaussian random variables with zero mean, all its statistical properties are contained in the variance  $C_\ell$ , also known as the power spectrum:

$$\langle a_{\ell m} a_{\ell' m'}^* \rangle = \delta_{\ell\ell'} \delta_{mm'} C(\ell), \quad (2.44)$$

where  $\delta_{mm'}$  is the Kronecker delta taking  $m$  and  $m'$  as arguments.

The fact that for lower values of  $\ell$  there are fewer coefficients  $a_{\ell m}$  naturally leads to lower multipoles  $\ell$  having higher uncertainty, this property is usually called cosmic variance and can be expressed using[33]

$$\left( \frac{\Delta C(\ell)}{C(\ell)} \right)_{\text{cosmic variance}} = \sqrt{\frac{2}{2\ell + 1}}. \quad (2.45)$$

The temperature autocorrelation defined in equation (2.44) is usually expressed as  $C_\ell^{TT}$ , but sometimes a modified spectrum  $D_\ell^{TT} = \frac{\ell(\ell+1)}{2\pi} C_\ell^{TT}$  is used for visualization purposes. Figure 2.2 shows Planck's CMB power spectrum data and its corresponding best-fit spectrum assuming a  $\Lambda$ CDM cosmology.

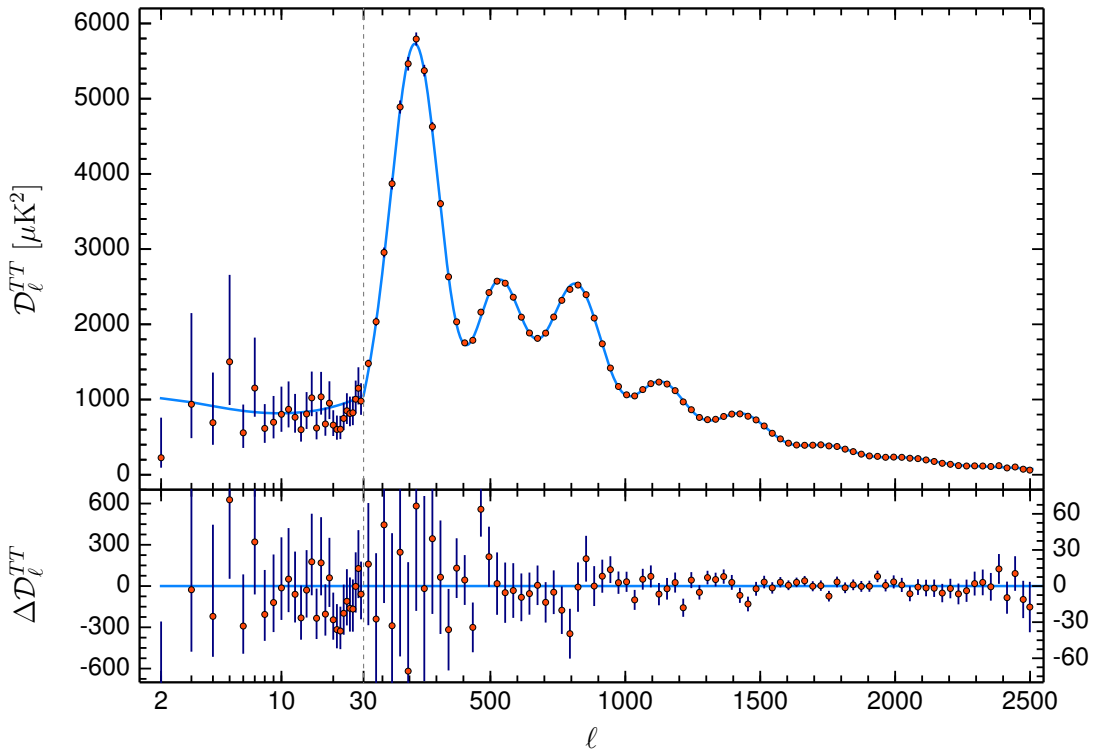


Figure 2.2: Planck 2018 CMB temperature power spectrum: the blue line corresponds to a  $\Lambda$ CDM cosmology best-fit to the data points in orange. For  $\ell < 30$  a logarithmic scale was used and the data points correspond to the  $D_\ell^{TT}$  for each value of  $\ell$ , while for  $\ell \geq 30$  a linear scale was used and the data points correspond to binned values for the data for  $D_\ell^{TT}$ . The error bars show  $\pm 1\sigma$  uncertainties, including cosmic variance. Extracted from [6].

Reference [6] also provides a table with the best fit values for cosmological parameters obtained by analysing the data shown in Figure 2.2, the values are shown in Table 2.2, except for the energy densities already shown in Table 2.1.

The best fit values shown in Tables 2.1 and 2.2 are the values that have been used in this project for the fiducial  $\Lambda$ CDM model.

Parameter	Best fit
$\Omega_b h^2$	0.02237
$\Omega_c h^2$	0.1200
$100\Theta_{MC}$	1.04092
$\tau$	0.0544
$\ln(10^{10} A_s)$	3.044
$n_s$	0.9649
$\Omega_m$	0.3135
$H_0$	67.36 km/s/Mpc
$\sigma_8$	0.8111

Table 2.2: Best fit values of cosmological parameters reported by the Planck collaboration using a combined likelihood with temperature and polarization spectra and lensing data. Here  $h = H_0/(100 \text{ km/s/Mpc})$  is the reduced Hubble constant,  $\Theta_{MC}$  is the angular scale of the sound horizon at the surface of last scattering,  $A_s$  is the amplitude of the primordial scalar perturbations,  $n_s$  is the spectral index of the primordial scale perturbations,  $\Omega_m = \Omega_c + \Omega_b$  is the matter energy density and  $\sigma_8$  measures the amplitude of density fluctuations at the scale of  $8h^{-1}$  Mpc. The first 4 parameters, alongside are used for solving the perturbation equations with CAMB and the last 3 are derived from the solution.

### 2.3.2 Analytical Approximation

Although solving equations such as (2.34) numerically gives accurate results, obtaining an analytical approximation to these equations helps us understand the underlying physical effects that most influence the evolution of the perturbations. Working on the tightly coupled limit and assuming recombination to be an instantaneous process happening at conformal time  $\eta = \eta_*$ , one can obtain the following equation[33]:

$$\begin{aligned} \Theta_\ell(k, \eta_0) \approx & [\Theta_0(k, \eta_*) + \Psi(k, \eta_*)] j_\ell[k(\eta_0 - \eta_*)] \\ & + iv_b(k, \eta_*) \left\{ j_\ell[k(\eta_0 - \eta_*)] - (l+1) \frac{j_\ell[k(\eta_0 - \eta_*)]}{k(\eta_0 - \eta_*)} \right\} \\ & + \int_0^{\eta_0} d\eta e^{-\tau} [\Psi'(k, \eta) - \Phi'(k, \eta)] j_\ell[k(\eta_0 - \eta)], \end{aligned} \quad (2.46)$$

where  $j_\ell$  are spherical Bessel functions, the conformal time  $\eta$  is defined as

$$\eta = \int_0^t \frac{dt}{a(t)}, \quad (2.47)$$

and  $\eta_*$  is the value of  $\eta$  that maximizes the visibility function  $g(\eta)$ :

$$g(\eta) = -\tau' e^{-\tau}. \quad (2.48)$$

With these conventions, the derivative with respect to  $\eta$  is being represented by the apostrophe notation, while the dot notation used in equation (2.34) will still indicate derivatives with respect to time.

There are three main contributors to the solution (2.46):

- The  $(\Theta_0 + \Psi)$  term is usually called the Sachs-Wolfe term, which is associated with Baryon Acoustic Oscillations (BAO), which are fluctuations in the density of the visible baryonic matter of the Universe, caused by acoustic density waves in the primordial plasma of the early Universe[33];
- The  $iv_b$  term shows a contribution to the spectrum related to a Doppler shift of the BAO, due to its dependence on a non-zero bulk velocity of the baryons during recombination;
- The last term, an integral involving the time variations of the gravitational potentials, represents the Integrated Sachs-Wolfe (ISW) effect. Its dependence on the variation of the gravitational potential makes it so that it only has a non-negligible effect on the CMB at cosmological periods with high variation of these potentials: At around  $a \approx 10^{-4}$  the Universe transitioned from a radiation-dominated to a matter-dominated Universe (early ISW), and recently – around  $a \approx 0.61$  or  $z \approx 0.63$ [47] according to the  $\Lambda$ CDM model – the Universe transitioned from a matter-dominated Universe to the current dark energy dominated Universe (late ISW).

## 2.4 The Integrated Sachs Wolfe Effect

It was proposed that the cross-correlation spectrum between CMB maps and matter contrast could be used to detect the ISW effect[48], and since then many works have reported the detection of this signal[22, 49–51]. In this section, a framework for theoretical estimations of the ISW contribution to this cross-correlation will be discussed.

### 2.4.1 The Matter Power Spectrum

While the CMB is usually described as a two dimensional map measured around the Earth, the matter distribution in the Universe is first analyzed taking the distance from the Earth into consideration, so three coordinates are necessary, and then one can take a 2D projection for a certain redshift  $z$ . Again using Fourier space, we first define the 3D matter power spectrum for the distribution of matter perturbations in the Universe  $P(k)$  as

$$\langle \delta(\mathbf{k}, z) \delta^*(\mathbf{k}', z) \rangle = (2\pi)^3 P(k, z) \delta_D(\mathbf{k} - \mathbf{k}'), \quad (2.49)$$

where  $\delta_D$  is the Dirac delta,  $\delta$  is the previously shown matter perturbation distribution in the Universe and the  $*$  superscript indicates the complex conjugate of a quantity. Again, using appropriate initial conditions, one can determine  $\delta(\mathbf{k})$  and thus  $P(k, z)$ , and again these results can be obtained numerically using CAMB, Figure 2.3 shows the results for this calculation.

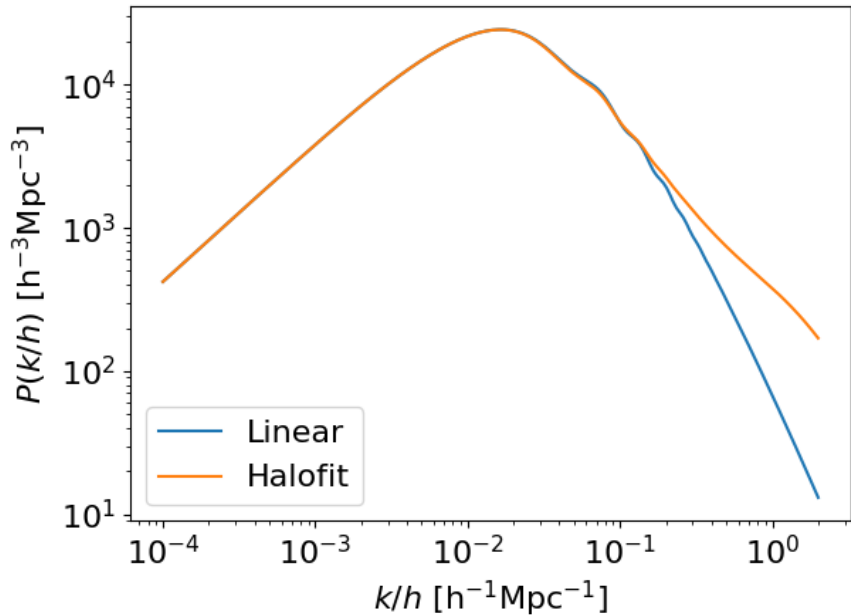


Figure 2.3: Matter power spectrum calculated as a function of  $k/h$ , where  $h$  is the already defined reduced Hubble constant, using both a linear approximation and the so-called HALOFIT model[52] with cosmological parameters according to our fiducial  $\Lambda$ CDM model.

The HALOFIT model is a semi-analytical method to determine a non-linear solution for  $P(k, z)$ , it is based in the Halo Model, which posits that all matter resides in haloes, and uses this hypothesis to describe the evolution of perturbations in the universe. The corrections due

to the HALOFIT model are not relevant in large scales, as shown in Figure 2.3, in which both spectra are indistinguishable at low values of  $k$ , only at higher values of  $k$  – small scales – the two spectra clearly diverge. In terms of the correlation power spectra, one can already notice a significant difference in the predicted spectra at around  $\ell = 40$ [24], showing very clearly the importance of using HALOFIT for our analysis.

### 2.4.2 The Galaxy-CMB Correlation Spectra

To obtain the autocorrelation for a spherical projection of a matter density distribution on a spherical shell on a certain redshift  $z$ , one has to choose a way to trace the matter density with an observable. One way of doing this is by tracing the mass distribution with galaxy density on a certain redshift. It is common to assume that the galaxy density perturbations, usually called galaxy contrast maps, take the form  $\delta_g = b_g \delta$  where  $b_g$  is a constant value (for each redshift  $z$ ) called the bias factor. From this point, the same process needed to calculate (2.44) can be applied: Expand the distribution in spherical harmonics with factors  $a_{\ell m}^g$  and calculate the variance of these variables to obtain an autocorrelation spectrum  $C^{gg}(\ell)$ .

Similarly, instead of calculating an autocorrelation spectrum, one can calculate a cross-correlation between two perturbation distributions, which is analogous to definition (2.44):

$$\langle a_{\ell m}^t a_{\ell' m'}^g \rangle = C_\ell^{tg} \delta_{\ell \ell'} \delta_{mm'}. \quad (2.50)$$

By using equation (2.41) one can express  $a_{\ell m}$  in terms of  $\Theta_\ell$ , which can be expanded using equation (2.46), this expansion and the correlation definitions allow us to find analytical expressions for all correlation functions discussed so far using the approximations discussed, but we can also use the ISW term in equation (2.46) to calculate the sole contribution of the ISW effect to the full correlation spectra.

In this work we have used the form shown in [24], which is specific to the ISW contribution to these correlation spectra:

$$C_\ell^{xy} = \frac{2}{\pi} \int dk k^2 W_\ell^x(k) W_\ell^y(k) P(k), \quad (2.51)$$

where  $x$  and  $y$  can represent  $g$  or  $t$ , and  $W_\ell$  are called the kernel functions, which can be calculated using

$$W_\ell^t = -3\Omega_m \left( \frac{H_0}{k} \right)^2 \int dz \frac{d[(1+z)D(z)]}{dz} j_\ell[k\chi(z)], \quad (2.52)$$

$$W_\ell^g = \int dz b_g(z) \frac{dN}{dz} D(z) j_\ell[k\chi(z)], \quad (2.53)$$

where  $D(z)$  is the linear growth function (normalized to 1 at  $z = 0$ );  $\chi(z)$  is the comoving distance; and  $\frac{dN}{dz}$  is the normalized galaxy redshift distribution, also called the selection function[49]. A demonstration of this equation can be found in Appendix B.

With equation (2.51), we can determine the theoretical spectra for CMB and galaxy autocorrelations and CMB-galaxy cross-correlation directly. Figure 2.4 shows the total CMB autocorrelation and the ISW contribution, both at  $z = 0$ .

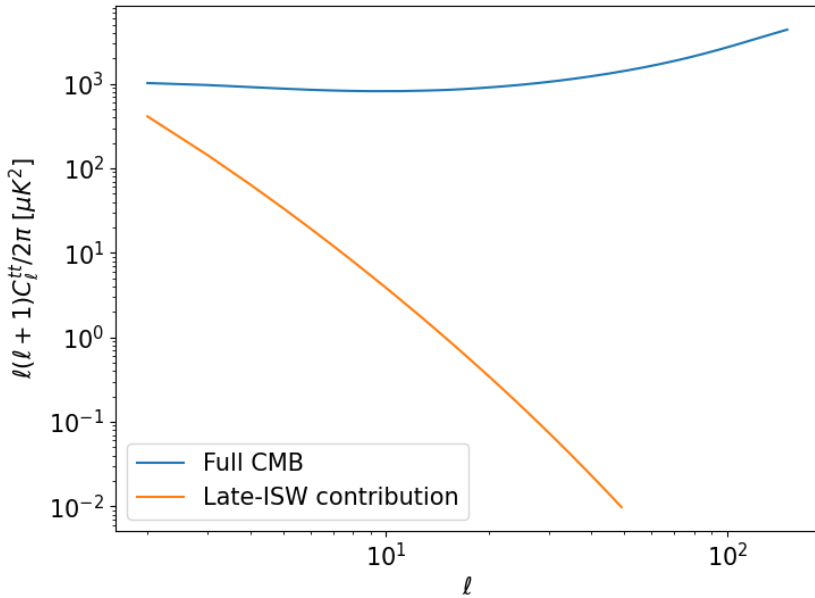


Figure 2.4: CMB autocorrelation comparison for the late-ISW term and the full spectrum. Calculations were made using CAMB (for the full spectrum) and codes developed during the project. The parameters used are those corresponding to the Planck best fit parameters[6].

Figure 2.5 shows the galaxy autocorrelation spectrum and the galaxy-CMB cross-correlation spectrum. All of these spectra have been integrated numerically.

These plots show very clearly that the ISW effect has a lot more relevance in the lower multipoles, where cosmic variance has a significant influence. The selection function is an important aspect of this signal, in chapter 3 the matter of how to optimize the signal with the use of an idealized selection function will be discussed.



Figure 2.5: Galaxy autocorrelation spectrum (left) and late-ISW contribution to the galaxy-CMB cross-correlation (right). The selection function used to calculate these spectra was parametrized to be compatible with 2MASS’ galaxy redshift distribution[24, 49].

## 2.5 Dependence on Dark Energy Models

Many approaches to study dark energy have been proposed, each of them with different properties, ranging from parameterization of the equation of state[53, 54] to alternative fluid models for dark energy[55, 56] and modifications to general relativity[57].

A general class of dark energy models are the ones called the k-essence models. The energy-momentum tensor for a k-essence type dark energy is

$$T_{\mu\nu} = \partial_X \mathcal{L} \nabla_\mu \varphi \nabla_\nu \phi - \mathcal{L} g_{\mu\nu}, \quad (2.54)$$

where  $\varphi$  is the k-essence scalar field and  $X = -\frac{1}{2}g^{\mu\nu}\partial_\mu\varphi\partial_\nu\varphi$  is a kinetic term. Equation (2.54) can be compared with the perfect fluid equation to obtain

$$\rho = 2X\partial_X \mathcal{L} - \mathcal{L}, \quad p = \mathcal{L}, \quad c_s^2 = \frac{\partial_X p}{\partial_X \rho}, \quad (2.55)$$

where  $c_s^2$  is the so-called sound speed of the k-essence fluid. The value of this parameter influences, for instance, the evolution of the gravitational potentials[58] and their perturbations – especially at low values of  $c_s$  – and many other factors that relate to the evolution of the universe, thus having an impact on observables.

Within k-essence, a very common class of models are the quintessence models, which are

defined by  $\mathcal{L} = X - V(\varphi)$ , for which we can obtain an equation of state parameter  $w = p/\rho$  and sound speed of

$$w = \frac{X - V}{X + V}, \quad c_s^2 = 1. \quad (2.56)$$

Equation (2.56) can be time dependent, and its form depends on the form of the potential  $V$ . Parametrizing this equation as a function of redshift and fitting it to the data can be a powerful tool to find what models might better describe dark energy. The simplest parametrization proposed for dark energy's equation of state is called the Chevallier-Polarski-Linder (CPL) parametrization[36, 53]:

$$w(z) = w_0 + \left(1 - \frac{1}{1+z}\right) w_a. \quad (2.57)$$

So far, this parametrization has not solved some of the current limitations being faced by the  $\Lambda$ CDM model, such as the Hubble tension [59] and the  $\sigma_8$  tension [6], it has not improved over the  $\Lambda$ CDM predictions, but it shows good compatibility with CMB, type IA supernovae and baryon acoustic oscillations (BAO) data[6]. Planck results using this parametrization are shown in Table 2.3.

Parameter	Marginalized Value
$w_0$	$-0.957 \pm 0.080$
$w_a$	$-0.29^{+0.32}_{-0.26}$
$H_0 [\text{km s}^{-1}\text{Mpc}^{-1}]$	$68.31 \pm 0.82$
$\sigma_8$	$0.820 \pm 0.011$
$\Delta\chi^2$	-1.4

Table 2.3: Marginalized values and 68% confidence limits for cosmological parameters, assuming parametrization (2.57), obtained by combining Planck temperature and polarization autocorrelation and cross-correlation spectra[60], type IA supernovae data from the Joint Light Curve Analysis (JLA)[61] and BAO data from the Sloan Digital Sky Survey (SDSS)[62]. The  $\Delta\chi^2$  value was computed with respect to the  $\Lambda$ CDM best fits computed from the same data set combination.

Figure 2.6 shows the influence of different parameter values, using the CPL parametrization, on the CMB temperature autocorrelation spectrum, and compares the expected theoretical spectra with Planck's data.

In Figure 2.6, it is important to note that  $w_a = 1$  is a very extreme scenario, where  $w_{de} = 0$  at

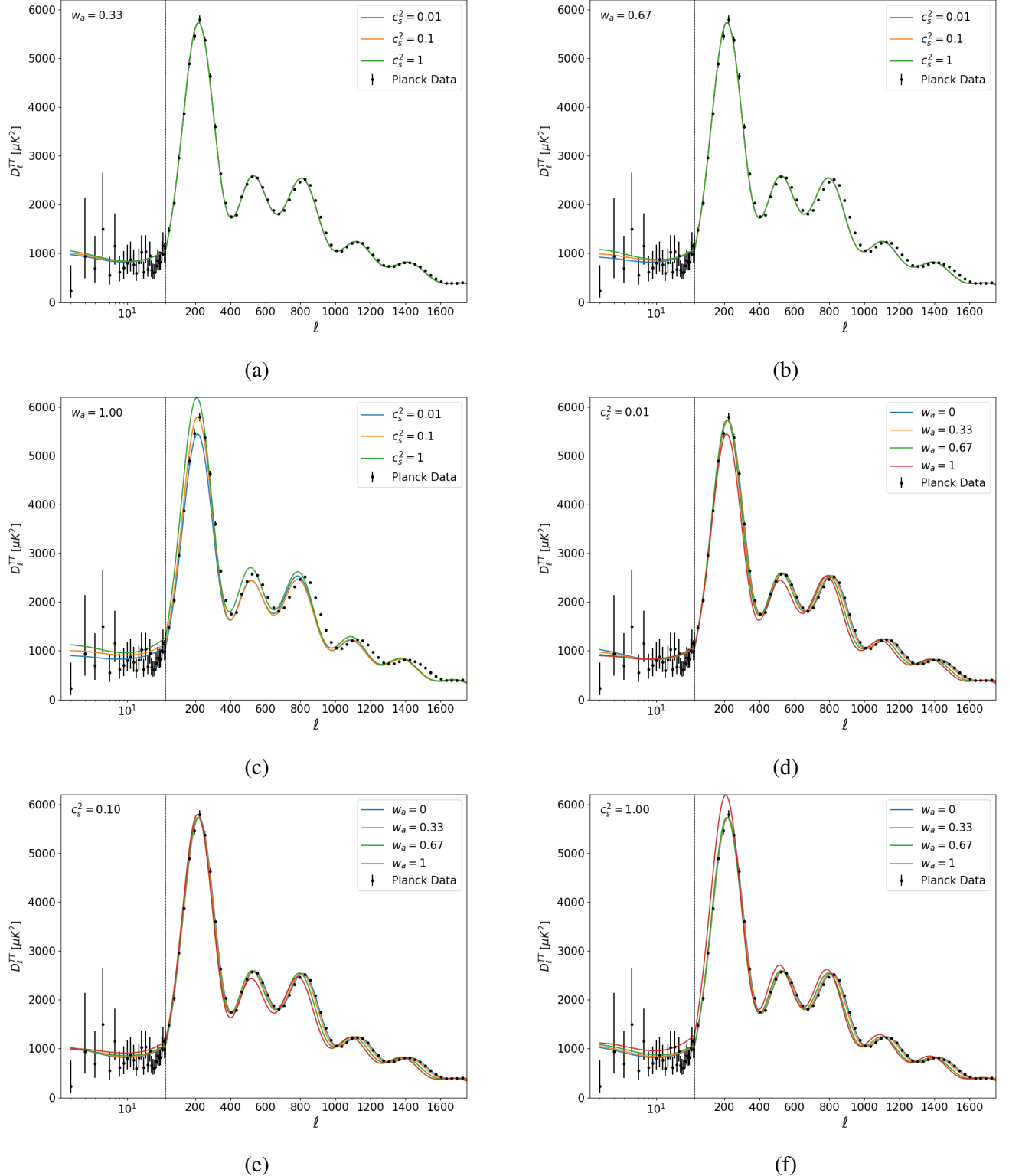


Figure 2.6: The solid lines in the plots correspond to theoretical predictions for the CMB temperature autocorrelation spectra corresponding to different parameter values of the dark energy equation of state with  $w_0 = -1$ , the black data points correspond to Planck's data[6]. Figures 2.6a, 2.6b and 2.6c show how the spectrum changes for a constant value of  $w_a$  shown on the top left of the axis and varying speeds of sound, while the other three figures show how the curve behaves with varying values of  $w_a$  and a constant speed of sound. All theoretical calculations were done using CAMB.

very high redshifts, meaning it would behave like matter, which is a behavior very incompatible with what's expected in the models. (reference?)

# 3 | Optimizing the Selection Function

Equation (2.53) introduced the selection function  $\frac{dN}{dz}$ , which simply corresponds to the redshift distribution of galaxy counts  $N$  and can vary depending on the galaxy catalog used, thus having an influence on the expected cross-correlation and galaxy autocorrelation signals that can be extracted from that catalog. As shown in Figure 2.5, the ISW signal is mostly present at low multipoles, where cosmic variance has a strong influence, making it hard to determine whether the data follow the model or the null hypothesis of zero cross-correlation. This motivated us to study the possibility of optimizing the cross-correlation signal by determining a selection function that could theoretically maximize it, this study will be presented in this chapter.

## 3.1 Parametrization of the Selection Function

Following [49], we are assuming the selection function can be parametrized as

$$\frac{dN}{dz}(z|\lambda, \beta, z_0) dz = \frac{\beta}{\Gamma(\lambda)} \left(\frac{z}{z_0}\right)^{\beta\lambda-1} \exp\left[-\left(\frac{z}{z_0}\right)^\beta\right] d\left(\frac{z}{z_0}\right) \quad (3.1)$$

where the parameters  $\beta$ ,  $\lambda$  and  $z_0$  are all positive. The values used to calculate the spectra in Figure 2.5 are those corresponding to the so called band 1 of the 2MASS infrared galaxy catalog. Table 3.1 shows the parameter values for each band of this catalog, while Figure 3.1 shows the plots for their corresponding selection functions. The details on what each of these bands represent will be presented in chapter 4.

Band	$z_0$	$\beta$	$\lambda$
1	0.043	1.825	1.524
2	0.054	1.800	1.600
3	0.067	1.765	1.636
4	0.084	1.723	1.684

Table 3.1: Parameter values for the 4 bands of the 2MASS catalog. Values extracted from [49].

To start the search for an ideal selection function, a good first guess would be to find functions that favor galaxies at redshifts close to the period of transition to the current dark energy dominated universe. The beginning of the period of accelerated expansion can be



Figure 3.1: Selection function calculated for the 4 bands of the 2MASS catalog according to equation (3.1).

calculated by inputting the  $\Lambda$ CDM values for cosmological parameters in the following equation

$$z^* = \left[ -(1 + 3w_{de}) \frac{\Omega_{de}}{\Omega_m} \right]^{-\frac{1}{3w_{de}}} - 1, \quad (3.2)$$

for which a demonstration is provided in Appendix A. If we use the values of Table 2.1, we obtain  $z^* \approx 0.63$ . By analysing Figure 3.1, it is possible to see that none of the 2MASS bands have peak sensitivity close to this redshift.

To determine the region in the parameter space that favors redshift  $z^*$ , a study of the influence of each parameter in the selection function was necessary. Figure 3.2 shows how the selection function varies with changes in each of its parameters.

Figure 3.2 shows that increasing the value of  $\lambda$  seems to shift the peak of the selection function towards higher redshifts without significantly changing the width of the curve, while increasing  $\beta$  seems to narrow the curve without significantly changing the position of the peak, and increasing  $z_0$  seems to increase both the position of the maximum and the width of the curve.

These observations make it easier to change the parameters and see their influence on the cross-correlation signal and helps to choose a region of the parameter space to explore, but to do so, the matter of how to quantify the quality of the signal has to be discussed.

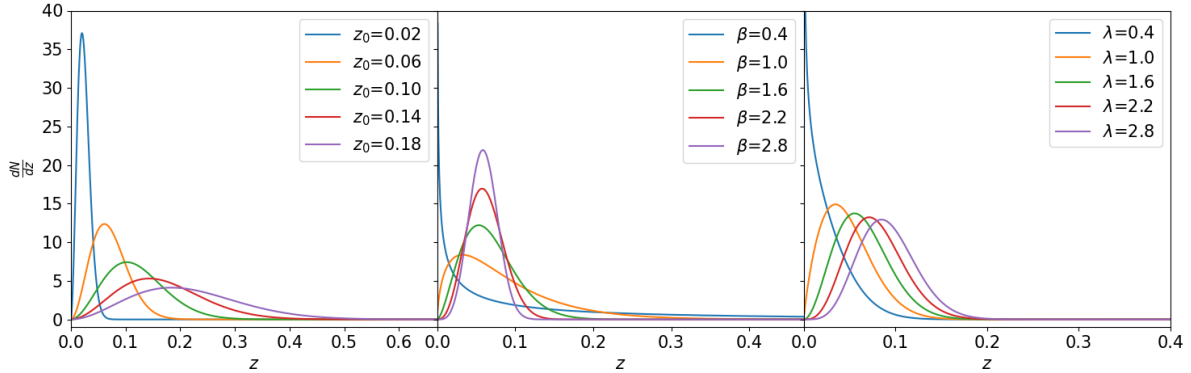


Figure 3.2: Selection function calculated for various parameter values according to the parametrization (3.1). Each plot is made by keeping 2 of its three parameters fixed, corresponding to the band 2 of the 2MASS catalog (see Table 3.1), the corresponding values of the varied parameter can be seen on the legend.

## 3.2 Maximizing the Cross-Correlation Signal

To maximize the signal we are in search of, we compare it with the null hypothesis, according to which there is no cross-correlation induced by the ISW effect, i.e  $C_\ell^{tg} = 0$  for every multipole. One way to do this is to synthesize multiple uncorrelated CMB temperature maps and galaxy contrast maps, calculate the power spectrum  $C_\ell^{tg}$  for each of them and, for each multipole  $\ell$ , determine the distribution of  $C_\ell^{tg}$ , using this as an estimation of the probability distribution of these cross-correlation samples.

In this part of the project, the HEALPix software was used extensively, and to validate the procedure for the search of the probability distribution for the null hypothesis, we first tested how the software would be able to retrieve the signal of a non-null cross-correlation spectrum. To do this, the full autocorrelation spectrum shown in Figure 2.4 calculated using CAMB was used alongside the correlation spectra shown in Figure 2.5 as inputs to *synfast*, a HEALPix harmonic space sampler and harmonic to real space map synthesizer. The synthetic maps generated with this procedure can then be decomposed into spherical harmonics coefficients  $a_{\ell m}$  using *anafast*, another HEALPix functionality. Figure 3.3 illustrates one galaxy contrast map and one CMB temperature map synthesized using this procedure.

Figure 3.4 shows a comparison between the theoretical correlation spectra and the ones estimated from averaging the correlation spectra of  $10^4$  synthetic maps, showing that among the three spectra considered here, the cross-correlation is the one most affected by cosmic variance.

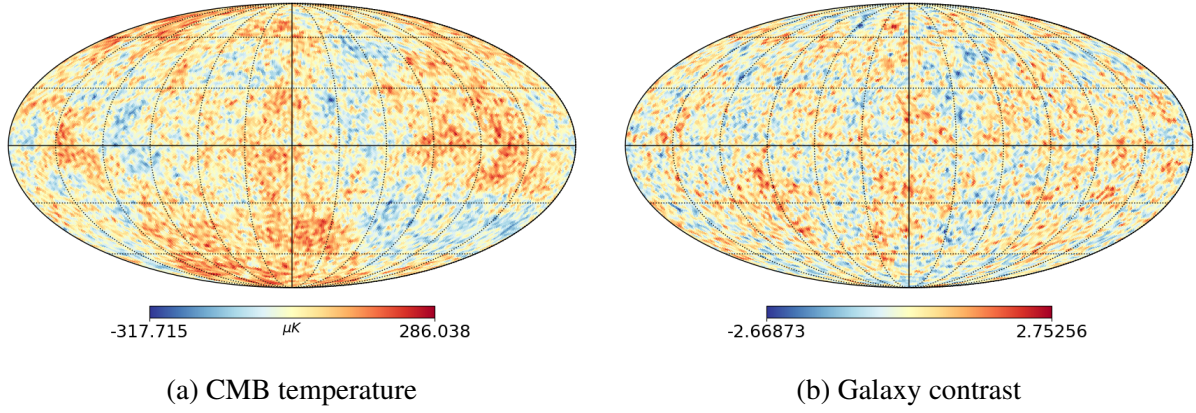


Figure 3.3: Mollweide projection of two instances of maps synthesized using HEALPix with the procedure presented.

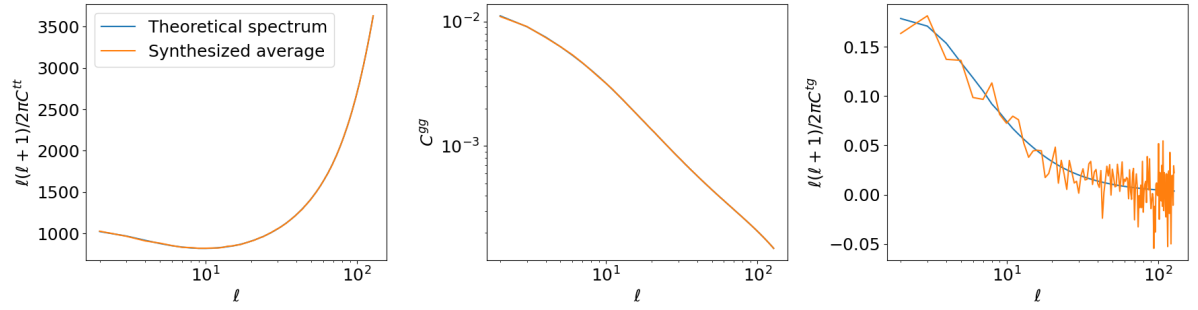


Figure 3.4: Comparison between theoretical auto and cross-correlation spectra and the averages of the  $C_\ell$  calculated from  $10^4$  synthesized maps using the procedure presented in this section.

In order to determine the probability distribution of the null hypothesis for each multipole, a similar process can be used, but now  $C^{tg}$  is set to zero, therefore, the temperature and galaxy contrast maps will be uncorrelated realizations of the autocorrelation spectra  $C^{tt}$  and  $C^{gg}$ . For each multipole, we have a sample of  $C_\ell^{tg}$ , one value for each map, the distribution of these values can be used as a probability distribution for the null hypothesis at each multipole. Figure 3.5 shows two histograms representing this distribution.

Upon thorough inspection of the histograms, we decided to fit each histogram using Gaussian distributions, which are shown in Figure 3.5, and used the fitted Gaussians as the probability density functions of  $C_\ell^{tg}$  under the null hypothesis. Each of these distributions will be indicated by  $f_\ell(C_\ell^{tg})$ , so

$$f_\ell(C_\ell^{tg}) = \frac{1}{\sqrt{2\pi}\sigma_\ell^2} \exp \left[ -\frac{1}{2} \left( \frac{C_\ell^{tg} - \mu_\ell}{\sigma_\ell} \right)^2 \right], \quad (3.3)$$

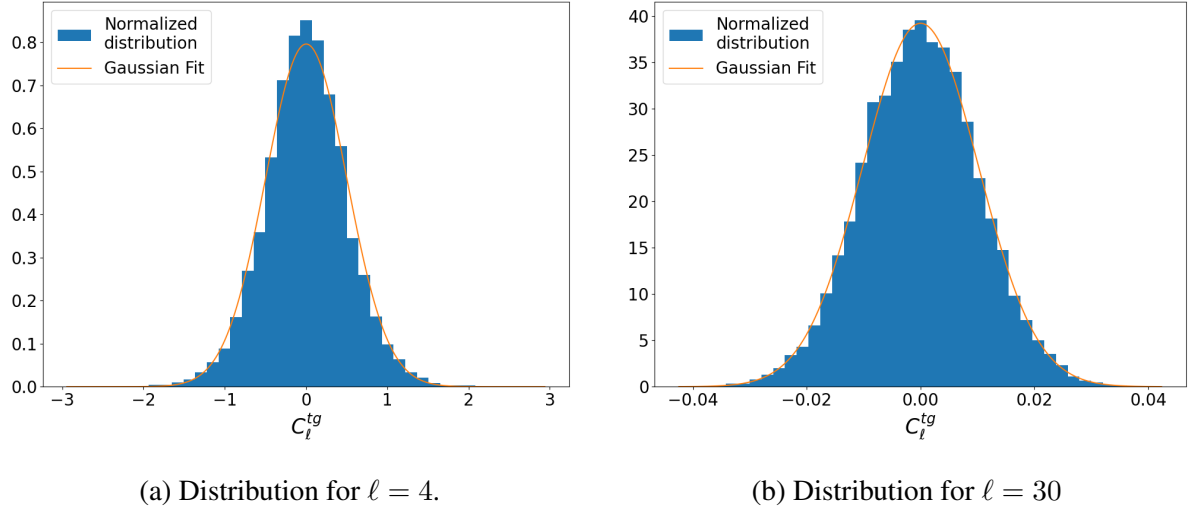


Figure 3.5: Distribution of cross-correlation values on different multipoles for  $10^4$  maps synthesized with null cross-correlation. Gaussian fits of the samples are shown alongside the normalized distributions. As expected, the averages of the distributions are close to zero, and the variance of the distribution is significantly higher in low multipoles due to cosmic variance.

where  $\sigma_\ell^2$  and  $\mu_\ell$  are the variance and average extracted from the distribution of  $C_\ell^{tg}$  shown in Figure 3.5.

With that, we can finally define the probability  $P_{\text{null}}$  that a correlation spectrum  $C^{tg}$  follows the null hypothesis:

$$P_{\text{null}} = \prod_{\ell=2}^{\ell_{\text{max}}} f_\ell(C_\ell^{tg}) \quad (3.4)$$

We can now explore the parameter space  $(z_0, \beta, \lambda)$  and look for the values that minimize  $P_{\text{null}}$ . In other words, for a given cosmological model chosen a priori (in this case  $\Lambda$ CDM) where a CMB-galaxy non-null cross-correlation signal is expected, what is the selection function that minimizes the consistency with a null signal.

To perform an initial exploration of the parameter space for the parametrization (3.1), 2D heat maps were produced by varying 2 of the 3 parameters while maintaining the third parameter fixed, the function mapped was  $P_{\text{null}}(z_0, \beta, \lambda)/P_{\text{null}}^{\text{2MASS}}$ , where  $P_{\text{null}}(z_0, \beta, \lambda)$  is the probability (3.4) calculated using power spectra computed with the selection function that corresponds to the given parameters, and  $P_{\text{null}}^{\text{2MASS}}$  is the same probability calculated with the parameters of the band 1 of the 2MASS catalog. Figure 3.6 shows examples of these heat maps.

As shown in Figure 3.6, the region explored does not present a significant reduction in the

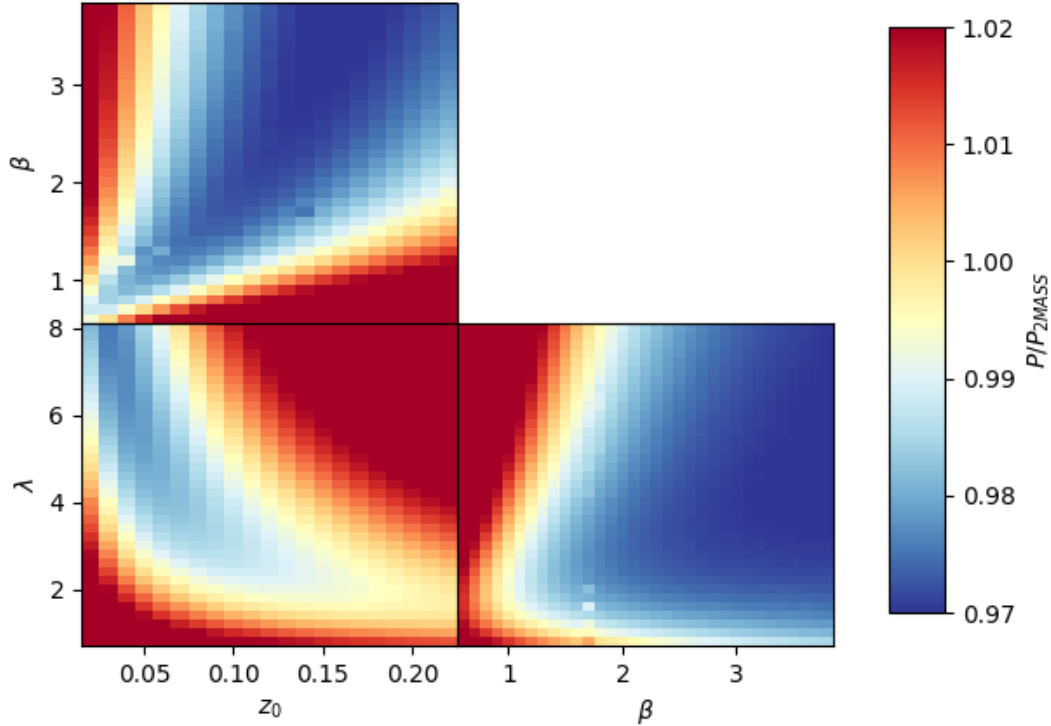


Figure 3.6: For each plot, one parameter is fixed at a certain value. The color of the plot indicates the ratio  $P_{\text{null}}(z_0, \beta, \lambda)/P_{\text{null}}^{\text{2MASS}}$ , according to the bar on the right. Dark blue regions indicate the lower values of this ratio, these are the regions that improve the signal according to our analysis, and can indicate regions where a minimum value can be found. The constant values are:  $\lambda = 5$  (upper left),  $\beta = 1$  (lower left) and  $z_0 = 0.17$  (lower right).

probability of a certain parameter combination being compatible with the null hypothesis relative to the band 1 of 2MASS, showing no more than a 3% reduction in the ratio. In spite of this, it is possible to see a region of low values for this function where a function minimizer algorithm could possibly be able to start the search for a minimum value.

A code for minimizing the function  $P_{\text{null}}$  using the GSL library[63] was devised, a few points were used as initial guess to the minimizer, some of them in the dark blue region, and some of them in the light blue regions, to make sure the convergence of the minimizer is reliable, and in every case results were very similar. The final value used for our analysis was

$$(\beta, z_0, \lambda)_{\min} = (3.088, 0.1508, 4.9401) \quad (3.5)$$

For this combination of parameters,  $P_{\text{null}}(z_0, \beta, \lambda)/P_{\text{null}}^{\text{2MASS}} = 0.971$ , still a 3% improvement relative to band 1 of 2MASS. Figure 3.7 shows the selection and cross-correlation functions

associated to the minimum of equation (3.5).

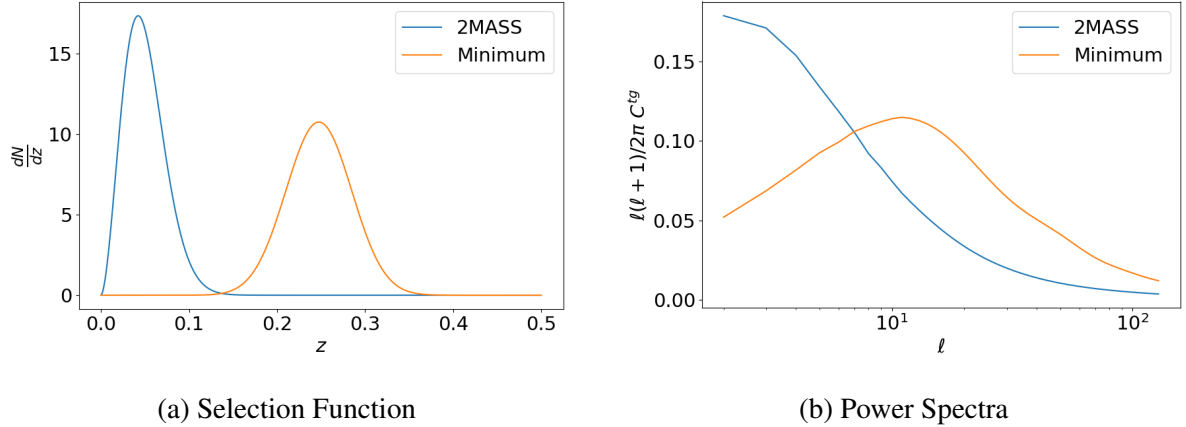


Figure 3.7: Comparison between theoretical properties of the point in parameter space that minimizes the null hypothesis and the band 1 of 2MASS.

The selection function shown in Figure 3.7a does not favor the predicted  $z^* = 0.63$ . This could possibly be reached by increasing the value of  $\lambda$ , but both the minimizer and the heat maps shown in 3.6 indicate that not much statistical value, if any, would be gained from doing so. The power spectra comparison in Figure 3.7b indicates an interesting tradeoff to achieve a better signal: it has a reasonably higher signal at around  $\ell = 10$ , where cosmic variance is not as relevant as it is around  $\ell = 2$ , but the function has a lower signal at its maximum point.

Despite these insights, the statistical gains from this ideal set of parameters are not very high compared with the 2MASS signal if we assume our galaxy catalog follows the parametrization (3.1) and that dark energy has a constant equation of state.

# 4 | Extracting Correlations from Data

CMB experiments do not directly measure correlation spectra, instead the data consists of time ordered data streams, each stream with information of the direction of observation and the sky temperature measured by that detector, which is contained within an array of detectors.

In this chapter, the process of converting this signal, taking into account the effects of detector noise and environmental variables such as the galactic background, will be discussed, not only for CMB but also for galaxy maps. A Monte Carlo Markov Chain (MCMC) algorithm capable of efficiently extracting these correlations, including the galaxy-CMB cross-correlation, will be presented.

## 4.1 Two Point Functions

To estimate any correlation spectrum, we first need to estimate the values of the multipole terms  $a_{\ell m}$ , but applying equation (2.44) to these directly does not yield accurate results, one has to introduce factors such as noise and map masks first.

In general, it is common to introduce a weight function  $W(\hat{\mathbf{n}})$  to account for various possible effects on the measured maps, such as galactic contamination, edge effects, and down-weighting more noisy pixels[64]. If we ignore other effects for now (such as noise), the multipole terms  $\tilde{a}_{\ell m}$  as defined in (2.43), assuming a high number of small pixels to approximate a sum with an integral, becomes

$$\tilde{a}_{\ell m} = \int d\Omega \Theta(\hat{\mathbf{n}}) W(\hat{\mathbf{n}}) Y_{\ell m}^*(\hat{\mathbf{n}}). \quad (4.1)$$

With this, one can define the so-called pseudo-power spectrum  $\tilde{C}_\ell$ :

$$\tilde{C}_\ell = \frac{1}{2\ell + 1} \sum_{m=-\ell}^{\ell} |\tilde{a}_{\ell m}|^2. \quad (4.2)$$

Still ignoring noise and other factors, one can relate the ensemble average of the pseudo-power spectrum with the true power spectrum with a simple system of equations

$$\langle \tilde{C}_\ell \rangle = \sum_{\ell'} M_{\ell\ell'} \langle C_{\ell'} \rangle, \quad (4.3)$$

where  $M_{\ell\ell'}$  is a matrix that describes the coupling between modes, called the multipole mixing matrix. If the mask applied to a CMB map is described by multipole functions  $\mathcal{W}_\ell$ , the mixing matrix corresponds to

$$M_{\ell\ell'} = \frac{2\ell' + 1}{4\pi} \sum_{\ell''} (2\ell'' + 1) \mathcal{W}_\ell'' \begin{pmatrix} \ell & \ell' & \ell'' \\ 0 & 0 & 0 \end{pmatrix}^2, \quad (4.4)$$

in which the term in parenthesis is a Wigner-3j symbol.

To find the full form of the system of equations used to determine the real power spectrum, one has to take into consideration the so-called beam pattern.

In radio astronomy, telescopes take measurements in various angles in the sky, and for each direction  $\hat{n}$ , there is an area of the sky being covered by the measurement, each of these areas is called a beam. In an apparatus that measures CMB photons' temperatures, the measurement in each direction  $\hat{n}$  is a temperature  $T^{\text{obs}}(\hat{n})$ , this measurement corresponds to a weighted combination of the real temperatures  $T(\hat{n}')$  over the beam:

$$T^{\text{obs}}(\hat{n}) = \int_{\text{beam}} d\Omega B(\hat{n}, \hat{n}') T(\hat{n}'). \quad (4.5)$$

The function  $B(\hat{n}, \hat{n}')$  is called the beam pattern, it weights the contributions of photons coming in the directions around the beam, and it can be estimated during the calibration of the apparatus, it is usually assumed to be Gaussian. Figure 4.1 shows the beam pattern for the Planck instrument at 30 GHz.

With the multipole terms  $B_\ell$  of the beam pattern  $B(\hat{n}, \hat{n}')$ , and given a noise map  $N$  that can also be expanded in multipoles  $N_\ell$ , the correlation functions can be extracted by solving the following system of equations:

$$\langle \tilde{C}_\ell \rangle = \sum_{\ell'} M_{\ell\ell'} B_{\ell'}^2 \langle C_{\ell'} \rangle + \langle N_\ell \rangle. \quad (4.6)$$

Although this solution converges to the true power spectrum in the limit of a large number of sky realizations, having a single universe to retrieve sky map multipoles makes this solution

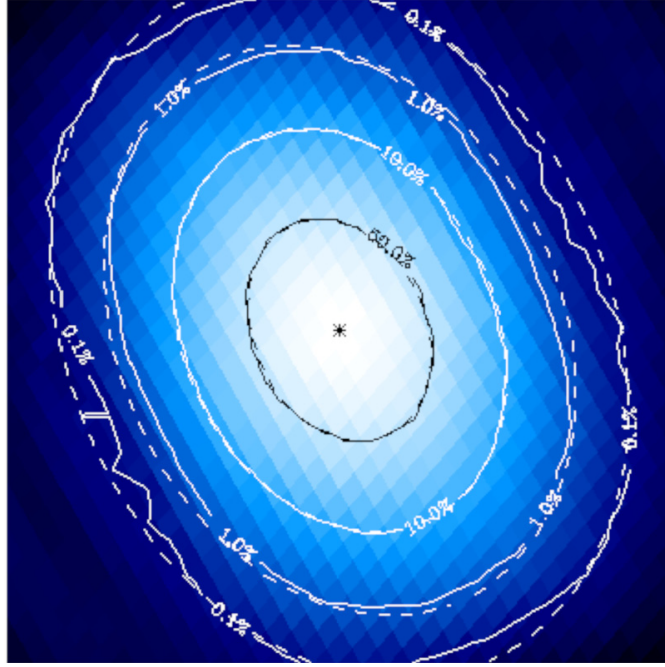


Figure 4.1: Beam pattern for the Planck instrument at 30 GHz. Contours delineate the regions where the beam function drops from its maximum to 50%, 10%, 1% and 0.1% respectively. Source: Planck wiki.

highly affected by cosmic variance[24]. Another limitation of this method is its computational complexity of  $O(N_p^3)$ , where  $N_p$  is the number of pixels of the sample maps. For experiments such as WMAP ( $N_p \sim 10^6$ ) and Planck ( $N_p \sim 10^7$ ), this time complexity becomes computationally unviable, thus motivating the introduction of a new technique, which will be presented now.

## 4.2 Gibbs Sampling

For a more efficient method than the one presented previously, Monte Carlo (MC) methods to sample maps of the primordial signal from the a posteriori probability distribution taking into account cosmic variance, instrumental noise, and residual foregrounds were developed[65–67].

Let  $d$  be a pixelized temperature map consisting of primordial signal  $s$  and instrumental noise  $n$ , both following Gaussian distributions with covariance matrices  $S$  and  $N$  respectively, with a full covariance matrix  $C = S + N$ . The likelihood for observing such a map, after marginalizing over the unknown signal  $s$ , can be calculated using

$$\mathcal{L} = P(\mathbf{d}|\mathbf{C}) = \frac{1}{(2\pi)^{n_{\text{dim}}/2} |\mathbf{C}|^{1/2}} \exp\left(-\frac{1}{2}\mathbf{d}^T \mathbf{C}^{-1} \mathbf{d}\right), \quad (4.7)$$

where  $n_{\text{dim}} = N_p^2$ . The direct evaluation of this likelihood is not computationally viable due to the calculation of the determinant of  $\mathbf{C}$ , a matrix that cannot be represented in diagonal form, since  $\mathbf{N}$  is typically close to diagonal in pixel space and  $S$  is diagonal in harmonic space.

Using Bayes' theorem, this likelihood can be written as  $P(\mathbf{C}|\mathbf{d}) \propto \pi(\mathbf{S})P(\mathbf{d}|\mathbf{C})$ , where  $\pi(\mathbf{S})$  is the prior on the power spectrum and  $P(\mathbf{C}|\mathbf{d})$  is the posterior probability density.

The calculation  $P(\mathbf{C}|\mathbf{d})$  can be done using an MC method called Gibbs sampling. Suppose we can sample from the conditional probabilities  $P(\mathbf{C}|\mathbf{s}, \mathbf{d})$  and  $P(\mathbf{s}|\mathbf{C}, \mathbf{d})$ , we can then sample a set of  $\{(\mathbf{s}^i, \mathbf{C}^i)\}$  by iterating the following sampling process[68]:

$$\mathbf{s}^{i+1} \leftarrow P(\mathbf{s}|\mathbf{C}^i, \mathbf{d}), \quad (4.8)$$

$$\mathbf{C}^{i+1} \leftarrow P(\mathbf{C}|\mathbf{s}^{i+1}, \mathbf{d}). \quad (4.9)$$

From this sample, one can use the so called Blackwell-Rao estimator to determine an approximation for  $P(\mathbf{C}|\mathbf{d})$ [68]. To construct this estimator, we first expand each element of the vector  $\mathbf{s}$  in terms of spherical harmonics:

$$\mathbf{s}(\theta, \phi) = \sum_{\ell=0}^{\infty} \sum_{m=-\ell}^{\ell} \mathbf{s}_{\ell m} Y_{\ell m}(\theta, \phi), \quad (4.10)$$

and define

$$\sigma_{\ell} = \frac{1}{2\ell + 1} \sum_{m=-\ell}^{\ell} \mathbf{s}_{\ell m} \mathbf{s}_{\ell m}^{\dagger}. \quad (4.11)$$

With this, it is possible to derive the Blackwell-Rao estimator for the density  $P(C_{\ell}|\mathbf{d})$ :

$$P(C_{\ell}|\mathbf{d}) \approx \frac{1}{N_G} \sum_{i=1}^{N_G} P(C_{\ell}|\sigma_{\ell}^i), \quad (4.12)$$

where  $N_G$  is the number of Gibbs samples and  $C_{\ell}$  are the multipole values due to the true signal  $\mathbf{s}$ .

In this project, the same process presented in [24], which is an extended version of what is presented in [69], has been used. In this framework, the vector  $\mathbf{s}$  and the matrix  $\mathbf{S}$  are defined as

$$\mathbf{s}^T = (s_{00}^{tg}, s_{01}^{tg}, s_{11}^{tg}, \dots, s_{\ell_{\max}0}^{tg}, \dots, s_{\ell_{\max}\ell_{\max}}^{tg}), \quad (4.13)$$

$$\mathbf{S} = \text{diag}(S_0^{tg}, S_1^{tg}, S_1^{tg}, \dots, S_{\ell_{\max}}^{tg}, \dots, S_{\ell_{\max}}^{tg}), \quad (4.14)$$

where

$$\mathbf{s}_{\ell m}^{tg} = \begin{pmatrix} a_{\ell m}^t \\ a_{\ell m}^g \end{pmatrix}, \quad \mathbf{S}_{\ell}^{tg} = \begin{pmatrix} C_{\ell}^{tt} & C_{\ell}^{tg} \\ C_{\ell}^{tg} & C_{\ell}^{gg} \end{pmatrix}. \quad (4.15)$$

It is also assumed that the noise's covariance matrix is diagonal:  $N = \text{diag}(N_{11}^{tg}, \dots, N_{ii}^{tg}, \dots, N_{pp}^{tg})$  where

$$N_{ii}^{tg} = \begin{pmatrix} N_{ii}^{tt} & 0 \\ 0 & N_{ii}^{gg} \end{pmatrix}, \quad (4.16)$$

since the noises affecting the temperature anisotropies and galaxy contrast are uncorrelated.

## 4.3 Data Sets and Analysis

In this project, we have used two main datasets for our analysis: CMB data from the Wilkinson Microwave Anisotropy Probe (WMAP)[5, 25] and galaxy contrast data from the Two Micron All Sky Survey (2MASS) catalog[26]. In this section, the details about these data sets and their respective analysis pipelines will be explored.

### 4.3.1 WMAP Data

WMAP used radiometers and differential microwave receivers to measure the CMB temperature over the entire sky across five frequency bands in the spectral region where the CMB-to-foreground ratio is near its maximum[25]. Out of these 5 frequency bands, we have used in this project the data corresponding to the Q (40GHz), V (60GHz) and W (90GHz) bands, which are the ones suitable for data analysis. Its last data release, WMAP9, which is the one used in this project, contains high resolution temperature intensity maps with noise power that can be well modeled as uncorrelated Gaussian fluctuations with variances given by  $\sigma_0^2/N_{\text{obs}}$ , where  $\sigma_0$  is a

parameter present in the data for each channel.

Figure 4.2 shows the maps used for the analysis with the so called KQ85 mask applied to them.

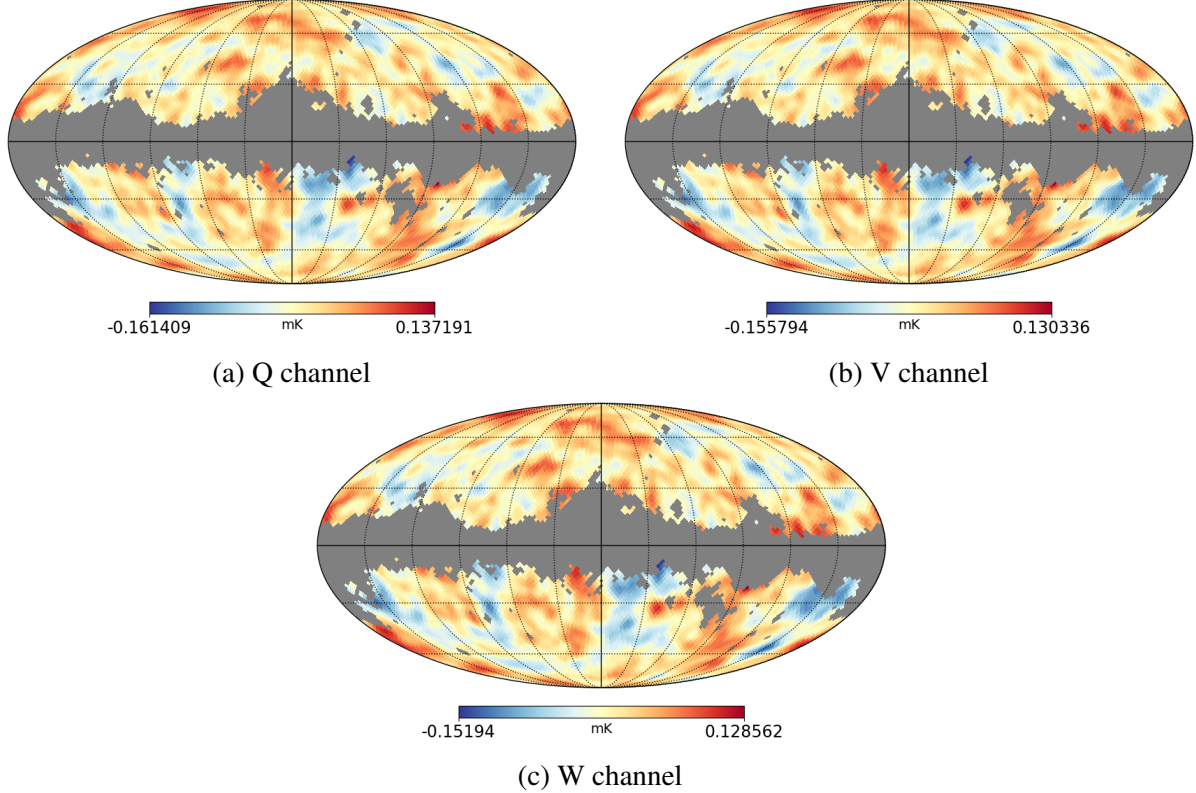


Figure 4.2: Mollweide projection of the 3 WMAP9 CMB temperature maps with the combined 2MASS+WMAP mask applied.

### 4.3.2 2MASS Catalog

From 1997 to 2001, the 2MASS collected raw imaging data covering 99.998% of the celestial sphere in three near-infrared bands: J ( $1.25 \mu\text{m}$ ), H ( $1.65 \mu\text{m}$ ) and  $K_s$  ( $2.16 \mu\text{m}$ ). This produced a Point Source Catalog containing more than  $4.7 \times 10^8$  point sources and an Extended Source Catalog (XSC) of 1, 647, 599 extended sources, which is the catalog we will use in this project to trace the galaxy contrast in the sky. This catalog contains sources that are extended with respect to instantaneous point source functions (PSF), such as galaxies and galactic nebulae.

The  $K_s$  band's 20 mag  $\text{arcsec}^{-2}$  isophotal circular aperture magnitudes (here simply called  $K_{20}$ ) were corrected for galactic extinction using the reddening maps  $E(B-V)$  at  $100 \mu\text{m}$  in [70], according to the expression  $K_{20} \rightarrow K'_{20} = K_{20} - A_k$ , where  $A_k = 0.367E(B-V)$ .

HEALPix was used to produce and analyse the maps with resolution parameter  $nside = 32$ , a mask was applied to every pixel with  $A_k > 0.05$ . This left the catalog at 801,476 objects with  $12 < K'_{20} < 14$ , which were further divided into the four bands: Bands 1 ( $12.0 < K'_{20} < 12.5$ ), 2 ( $12.5 < K'_{20} < 13.0$ ), 3 ( $13.0 < K'_{20} < 13.5$ ) and 4 ( $13.5 < K'_{20} < 14.0$ ).

This catalog is made using photometric measurements, meaning redshift information is not directly obtained with the measurements, but there are techniques to estimate photometric redshifts. In [71] the luminosity function of 4192 2MASS galaxies were used to estimate the luminosity function of the entirety of the  $K_s$  band, and then the photometric redshifts of these galaxies. In [72] the authors trained a neural network and cross-correlated XSC with WISE[73] and SuperCOSMOS[74] to obtain the photometric redshifts of a big fraction of the sources in XSC, creating what is called the 2MPZ catalog. As shown in [24], using the 2MPZ catalog over XSC does not yield significant changes in the results, so in this project we maintained the usage of the XSC data.

As explained in section 3.1, the redshift distribution of galaxy counts can be parametrized using the selection function defined in equation (3.1), the parametrizations for each band is shown in Table 3.1 and the plots of these selection functions is shown in Figure 3.1. Figure 4.3 shows the final maps produced after this process.

## 4.4 Correlation Spectra Obtained

It was verified in [24] that fixing the monopole and dipole terms at 0 in the Gibbs chain results in anomalous states at those scales, so the WMAP9 maps were decomposed, and the results obtained for  $C_0^{tt}$  and  $C_1^{tt}$  were taken and fixed along the chain. A study of the systematic errors was also made in the same reference.

To estimate the cosmic variance contribution on a masked map, or any map without full sky coverage, equation (2.45) has to be modified to take into account the effective sky fraction  $f_{\text{sky},\ell}$ , obtaining the following equation for the cosmic variance affecting  $C_\ell^{xx}$  of the given spectrum[75]:

$$(\Delta C_\ell^{xx})_{\text{cv}} = \frac{C_\ell^{xx}}{f_{\text{sky},\ell}} \sqrt{\frac{2}{2\ell + 1}}. \quad (4.17)$$

Here,  $C_\ell^{xx}$  can be substituted by either  $C_\ell^{gg}$  or  $C_\ell^{tt}$ , but it can also be substituted by  $D_\ell^{tt} = \ell(\ell + 1)/2\pi C_\ell^{tt}$  in both sides of the equation. For the cross-correlation  $C_\ell^{tg}$ , the equation is

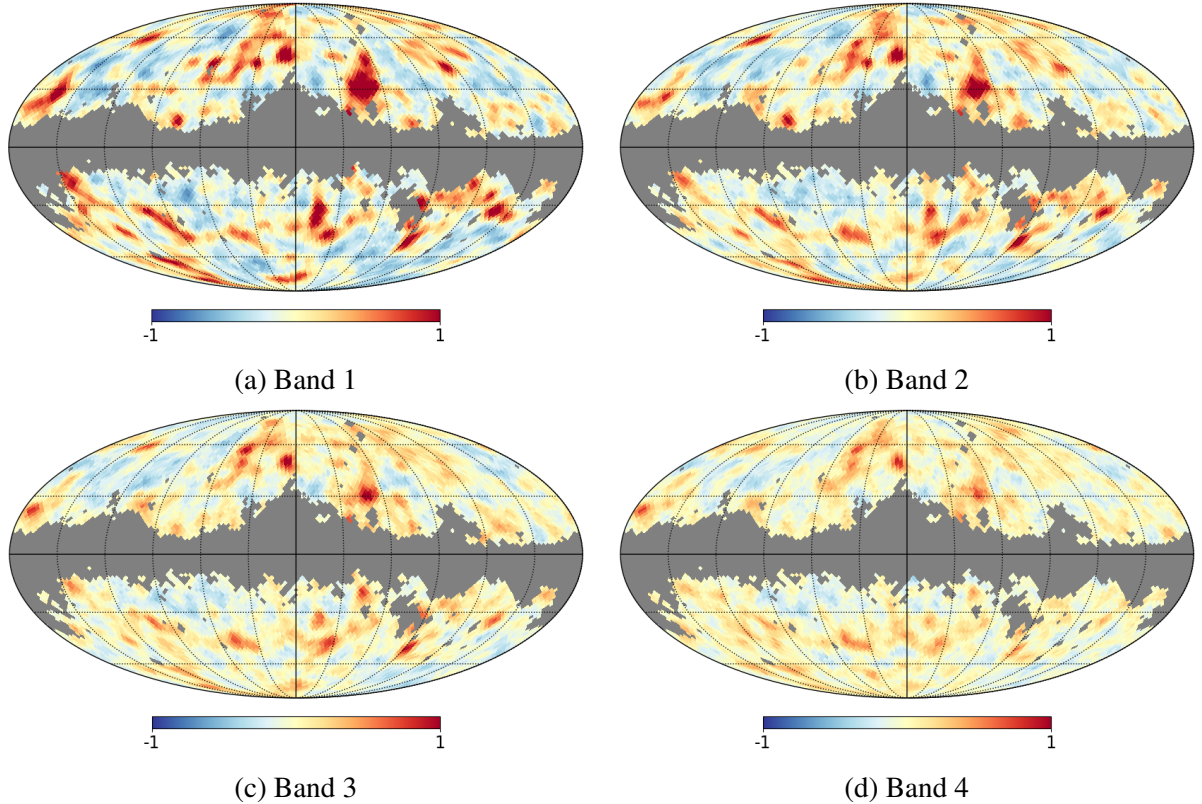


Figure 4.3: Mollweide projection of the 2MASS-XSC galaxy contrast maps with the combined 2MASS+WMAP mask applied.

adapted to

$$(\Delta C_\ell^{tg})_{cv} = \sqrt{\frac{2}{2\ell + 1} \frac{C_\ell^{tt} C_\ell^{gg} + (C_\ell^{tg})^2}{f_{sky,\ell}^2}}. \quad (4.18)$$

The procedures discussed so far in this chapter have already been done, more specifically the Gibbs sampling has already been done in [24] and all the data has been digitally stored and provided to be used in this project. Figure 4.4 shows a comparison between the theoretical correlation spectra and the ones calculated from the 2MASS+Q, V, W channels' data, alongside cosmic variance bands.

Figure 4.4 clearly shows that cosmic variance strongly dominates the signal at low multipoles, the region that is most influenced by the ISW effect.

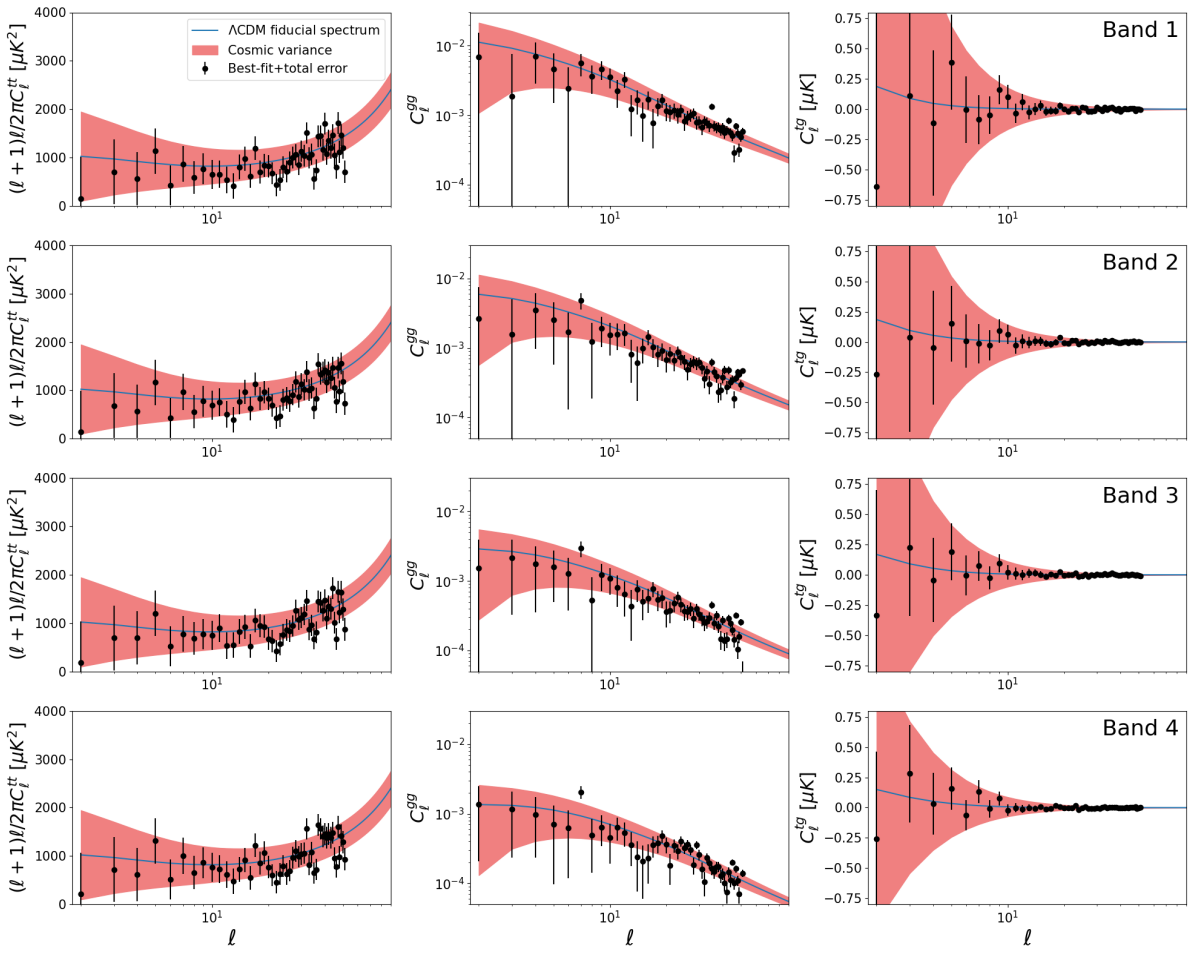


Figure 4.4: Comparison of theoretical correlation spectra for each band of the 2MASS catalog and the estimated correlation values using the method presented in the current chapter. Data points with error bars are the weighted average for channels Q, V, and W, with weights given by the reciprocal of noise variances. The red band corresponds to the cosmic variance, calculated using equations (4.17) and (4.18).

# 5 | Cosmological Constraints

With the data points and theoretical spectra shown in Figure 4.4, one can find new constraints for cosmological parameters. At first, we attempted to use an MCMC method with the Python package Cobaya[76, 77] to determine the constraints of multiple parameters, but I was not able to implement our theoretical estimation with Cobaya efficiently, so we decided to calculate the likelihood profile for  $\Omega_m$ , allowing us to analyse the influence that the cross-correlation data has on constraints of this parameter.

This limitation led us to instead calculate the likelihood profile for  $\Omega_m$  only, allowing us to analyse the influence that the cross-correlation data has on constraints of this parameter.

## 5.1 Monte Carlo Markov Chains

The usage of MCMC methods for analysing data has become a standard practice in recent years. While traditional direct evaluation methods usually rely on inverting complex matrix expressions and constantly having to renormalize the distributions being used, expressions that sometimes might not be analytically tractable and numerically unviable, MCMC methods sample values for a parameter – or multiple parameters – based on simple probability distributions that only need to be proportional to the exact probability distribution of the parameters given the data. Not only that, but having a set of parameters instead of a direct distribution function simplify both the process of visualizing the joint distribution of two parameters and the calculation of percentile intervals.

In a very general sense, three main probability functions are required to run an MCMC algorithm for this type of problem:

- The joint-likelihood function: The joint-likelihood function  $\mathcal{L}(Y|\theta)$  is the probability that the data points  $Y$  follow the model for a certain set of parameters  $\theta$ . As stated before, one does not need to normalize this function for the MCMC, this distribution will heavily depend on the properties of the dataset and the instruments;
- The prior distributions: A prior distribution on the parameters  $p(\theta)$  may be assumed, possibly based on the physical properties of the parameters. It also does not need to be

normalized;

- The proposal distribution: This probability will determine the transition probability from one point of the chain to the next, which – to satisfy the so called Markov property – only depends on the current state of the chain. Usually a Gaussian distribution is used as the proposal.

The stationary distribution of the chain will be the posterior distribution

$$P(\theta|Y) = \mathcal{L}(Y|\theta)p(\theta), \quad (5.1)$$

of a certain set of parameter values being the correct description of the data  $Y$ . In traditional methods, the normalization of this posterior distribution would be necessary for calculations of important statistical results, which can be unviable in many situations, especially if  $\theta$  is a set of many parameters. Using this as the stationary distribution of the Markov chain using the adequate methods (such as the Metropolis-Hastings algorithm[78]) does not require it to be normalized, and having a set of parameter values simplifies the calculation of the same statistical properties.

Two other important aspects of this procedure are the burn-in phase and the lagging. Despite the fact that for an infinite number of steps in the chain the distribution converges, when dealing with a finite number of steps, the first steps of the chain can create a bias in the sample, so it is common practice to discard the first points of the chain, this initial convergence phase is called the burn-in phase. Also, each step is highly correlated with its previous steps, which can also create bias, so a number of points in between two points can also be discarded to further reduce bias, this is called the lagging.

Cobaya is a Python package designed to run MCMC chains to analyse any type of data desired, but it is integrated with many sets of cosmological datasets and packages, such as Planck's data and CAMB, so it is more often used as a tool for analysis of cosmological data. Figure 5.1 shows the constraints at 68% and 95% for a chain using data and likelihoods provided by the Planck collaboration, using the  $\Lambda$ CDM model.

Cobaya uses the Gelman-Rubin Diagnostic[79] to test the convergence of the chains. We have used the  $R - 1 = 10^{-3}$  criteria for the convergence of the chains.

To determine the parameter constraints that can be obtained from the correlation spectra

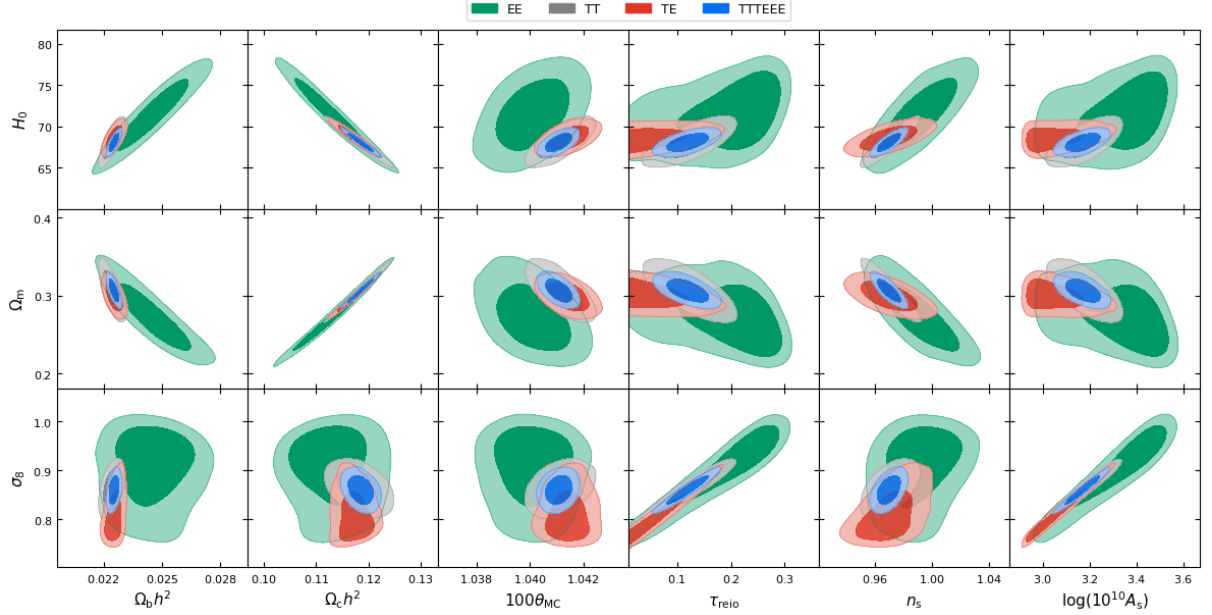


Figure 5.1: Joint posterior distributions of cosmological parameters using Planck’s CMB temperature (T) and polarization (E) data. The TTTEEE dataset combines both autocorrelation data (TT and EE) and the cross-correlation data (TE).

discussed so far, we have used the points shown in Figure 4.4 as data points. The theoretical calculations had to be integrated with Cobaya, so we have created a Python code capable of calling the C++ functions we have used to calculate the theoretical correlation spectra, which allowed us to integrate both codes.

## 5.2 Likelihoods

With the integrated code, we can calculate the theoretical correlation spectra  $C_{\ell, \text{theo}}^{xy}$  via a Python script,  $C_{\ell, \text{theo}}^{xy}$  can correspond to either CMB temperature or galaxy autocorrelation spectra, or the CMB-galaxy cross-correlation spectrum. For any of these cases, we have used the results shown in Figure 4.4 as data points  $C_{\ell, \text{data}}^{xy}$  to calculate the probability of the  $\Lambda$ CDM model describing the data for a certain set of parameters.

We have assumed that for each multipole  $\ell$  and for all the three different spectra, the likelihood is a Gaussian distribution of the form

$$\mathcal{L}(C_{\ell, \text{theo}}^{xy} | C_{\ell, \text{data}}^{xy}) = \frac{1}{\sigma_\ell \sqrt{2\pi}} \exp \left[ -\frac{1}{2} \left( \frac{C_{\ell, \text{data}}^{xy} - C_{\ell, \text{theo}}^{xy}}{\sigma_\ell} \right)^2 \right], \quad (5.2)$$

where  $\sigma_\ell$  are the errors of  $C_\ell^{\text{data}}$ . Before trying to run a chain varying all the cosmological parameters of interest, we decided to test the results of the procedure varying only  $\Omega_m$ . Since the only theoretical parameter being varied is  $\Omega_m$ ,  $C_\ell^{\text{theo}}$  is basically a function of  $\Omega_m$ , and so is the likelihood of each point. The combined likelihood of a single correlation spectrum is a product of the likelihoods of each multipole:

$$\mathcal{L}(\Omega_m | C_{\text{data}}^{xy}) = \prod_{\ell=2}^{\ell_{\max}} \mathcal{L}(C_{\ell, \text{theo}}^{\text{xy}} | C_{\ell, \text{data}}^{\text{xy}}). \quad (5.3)$$

We have analysed the likelihoods relative to both  $C^{tg}$  and  $C^{gg}$ , as well as their joint-likelihood:

$$\mathcal{L}(\Omega_m | C_{\text{data}}^{tg}, C_{\text{data}}^{gg}) = \mathcal{L}(\Omega_m | C_{\text{data}}^{tg}) \mathcal{L}(\Omega_m | C_{\text{data}}^{gg}). \quad (5.4)$$

Equation (5.4) is calculated in each band of the 2MASS catalog, the results can be normalized with respect to the maximum value obtained for each band, or multiplied to form a full 2MASS joint-likelihood of all 4 bands and then normalized with respect to the maximum value.

The likelihoods calculated using  $C^{tg}$  data from all 4 2MASS bands and the combination of all bands' likelihoods are shown in Figure 5.2.

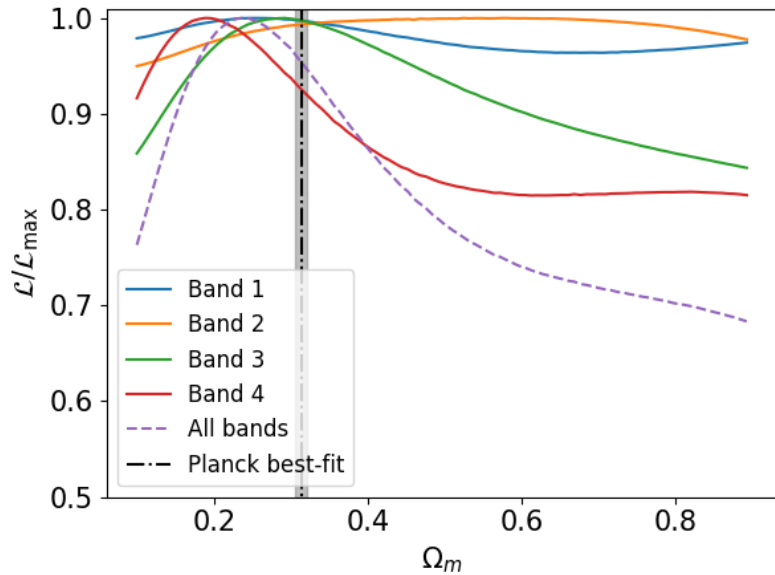


Figure 5.2: Normalized  $C^{tg}$  likelihood of each band of the 2MASS catalog and combination of all bands' likelihoods. The Planck best-fit for  $\Omega_m$  is shown for comparison, the gray band represents represents the 68% error.

Figure 5.2 shows that the CMB-galaxy cross-correlation data from 2MASS does not significantly constraint the  $\Omega_m$  parameter, the likelihoods calculated for every physically meaningful value of  $\Omega_m$  are within 70% of the maximum likelihoods obtained.

Bands 3 and 4 of 2MASS seem to have a higher constraint capability compared with bands 1 and 2. As shown in Figure 3.1, these bands contain galaxies in higher redshifts compared to the other two, which can be interpreted as another indication that using a galaxy catalog containing measurements of galaxies at higher redshifts may lead to a cross-correlation signal with a higher constraint power.

Figure 5.3 shows the  $C^{tg} + C^{gg}$  joint-likelihood calculated for each of the 4 bands of the 2MASS catalog, as well as the full 2MASS joint-likelihood of all the bands together.

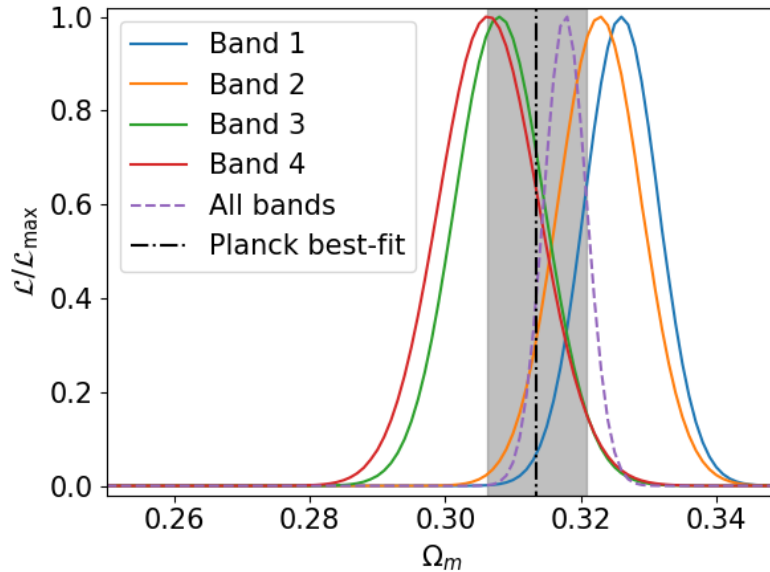


Figure 5.3: Normalized  $C^{tg} + C^{gg}$  joint-likelihoods for each band of the 2MASS catalog and full joint-likelihood of all bands. The Planck best-fit for  $\Omega_m$  is shown for comparison, the gray band represents represents the 68% error.

Simply visualizing the gray band and comparing it with the peaks of the likelihoods indicate that all bands and the full joint-likelihood are compatible with Planck's results, with bands 3 and 4 and the joint-likelihood having higher compatibility at less than  $1\sigma$ . The width of the likelihoods in all bands are very similar, showing very little differences between the constraint power of each band in this analysis.

Comparing these results with Figure 5.2 shows that  $C^{gg}$  has a much higher constraint power over  $\Omega_m$  than  $C^{tg}$ : while Figure 5.3 shows very narrow peaks in a very small region of the  $\Omega_m$

space, with nearly null likelihoods outside of this small region, while the results for  $C^{tg}$  show very high relative likelihood values across all physical values of  $\Omega_m$ , as previously discussed.

The width of the curves obtained in this project, using only  $C^{tg}$  and  $C^{gg}$  data, is comparable to the 68% Planck error for  $\Omega_m$ , showing that the combination of these two spectra have a very strong constraint power with respect to this parameter. It is important to highlight that this analysis only uses one variable parameter, while Planck's analysis used 6. If this analysis had been done with the same variable parameters, the width of the likelihoods would certainly increase, reducing the quality of the constraints, but increasing the compatibility with Planck's results. Despite this,  $C^{gg}$  is highly dependent on  $\Omega_m$ , so this increase would probably not be so high.

We have also performed an analysis using synthetic data following the optimized selection function discussed in Chapter 3. To do so, we have used a fiducial  $\Lambda$ CDM spectrum  $C_\ell^{tg}$  as data points, we have used the errors of 2MASS' band 4 as errors for this sample. Only the cross-correlation spectrum was used in this analysis. The results of this procedure are shown in Figure 5.4.

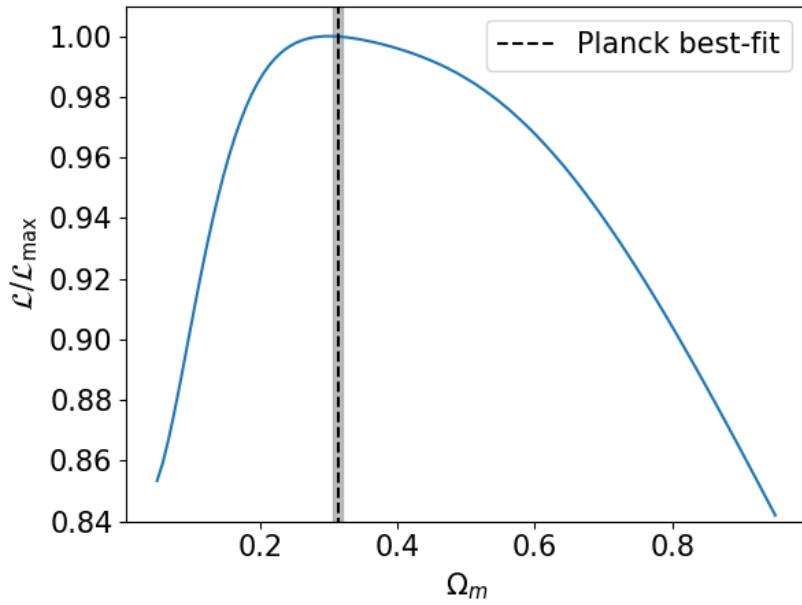


Figure 5.4: Normalized  $C^{tg}$  likelihood calculated using synthetic data estimated as the theoretical cross-correlation obtained using the idealized band estimated in Chapter 3 for the selection function, with 2MASS' band 4 errors. The Planck best-fit for  $\Omega_m$  is shown for comparison, the gray band represents represents the 68% error.

The range of the relative likelihood shown in Figure 5.4 is similar to those shown for bands

3 and 4 of 2MASS in Figure 5.2, and the width of the curve is higher in the current analysis, suggesting that this optimal band does not hold a stronger constraint power over  $\Omega_m$  at least.

It is important to remind that the analysis made in Chapter 3 we have found a parametrization of the selection function that locally maximizes the likelihood of the theoretical spectrum relative to the null hypothesis that there is no cross-correlation spectrum, not the parametrization that improves the constraint power relative to  $\Omega_m$ . Despite this, the null hypothesis is a result of  $\Omega_m = 1$  since the gravitational potentials would not vary in such a universe[80], thus rejecting the null hypothesis likely rejects very high values of  $\Omega_m$ .

Another similar work has been done in [81], in which the authors also analysed the 2MASS+WMAP cross-correlation signal, also finding a very low preference towards the non-null cross-correlation hypothesis, and studied whether new changes in the data sets could possibly improve the signal, such as greater galaxy survey depths and fainter magnitude limits, and reported that even with the best possible data in these frameworks, the signal would still evade detection in  $> 10\%$  of cases.

## 5.3 MCMC Convergence

In order to run the analyses in a reasonable amount of time, we have used both the Cobaya parallel implementation and a parallelization in the calculation of the theoretical spectra. Despite our efforts to run the code efficiently in USP's Aguia Cluster, our tests running the code varying only  $\Omega_m$  have resulted in chains with a very low acceptance rate, making it unviable for us to run the chains in a reasonable time frame. We have tried running the chains using only  $C^{tg}$  data and the combination  $C^{tg} + C^{gg}$ , both showing this limitation.

UNDERSTAND REASONS FOR THIS ACCEPTANCE RATE (ronaldo falou que as likelihoods mt flat resultam nisso mas na minha cabeça devia ser o contrário).

## 6 | Conclusions

In this work we have studied the possibility of using the integrated Sachs-Wolfe effect as a probe for analysing cosmological data. More specifically, we have studied the properties of the cross-correlation spectrum between a CMB temperature map and a galaxy contrast map. The method used to obtain this spectrum from the corresponding maps has already been tested and validated in [24], as discussed in Chapter 4, and although the signal was obtained, it was nearly indistinguishable from a zero cross-correlation hypothesis. As discussed, this difficulty arises from the fact the the ISW signal is mostly present at low multipoles, meaning there is a very high irreducible error contribution from cosmic variance.

In an attempt to solve this, we first studied if a hypothetical galaxy survey with an idealized redshift distribution could possibly improve the signal in a way that would distinguish it from the null hypothesis. Finally, we have obtained constraints for the  $\Omega_m$  parameter using the 2MASS+WMAP data, and did the same with artificial data corresponding to the idealized galaxy survey discussed before.

In chapter 3 we have studied the impact of the galaxy redshift distribution – here called the selection function – of a catalog in the cross-correlation signal. We have used a common parametrization for the selection function that uses 3 parameters, and analysed the impact of each parameter in the selection function (see Figure 3.2), which allowed us to control and search for a selection function that improves the cross-correlation signal, meaning this idealized galaxy catalog would maximize the likelihood function of the cross-correlation data relative to the null hypothesis that it is zero for all multipoles.

We have estimated the redshift at which the Universe started its accelerated expansion and opted to start searching the idealized selection function around that region. To do so, heat maps were produced in order to search for regions in the parameter space that might contain a minimum value. Figure 3.6 shows one of the most promising regions we have found, from which we have chosen a starting point to run an algorithm to minimize the likelihood function. Despite some promising properties of the idealized parametrization found (see Figure 3.7), the null hypothesis' likelihood in the optimal band is only 3% lower than that of 2MASS' band 1.

In Chapter 4 the matter of how to extract the correlation functions from data maps was

discussed, in which the process presented in [24] was presented alongside the final results of its application to the 2MASS galaxy catalog and the WMAP CMB temperature map, which are shown in Figure 4.4. The points shown are used as data points for the data analysis.

In Chapter 5, we discuss the usage of an MCMC approach to analyse the data obtained previously. The likelihood functions used are discussed and their profiles are obtained as a function of the  $\Omega_m$  parameter, maintaining all other parameters fixed. These likelihoods were used for the MCMC analysis using  $\Omega_m$  as the only varying parameter at first, and this process that was supposed to be simpler resulted in chains with a very low acceptance rate, which made the MCMC approach unviable in this work. Because of this, we use the likelihoods as a means of analysing the data.

Figure 5.2 shows this likelihood for all 2MASS bands using only the  $C^{tg}$  data, clearly demonstrating a very low variations in the curves, meaning very poor constraints over the varied parameter, and showing a better constraining power from bands 3 and 4. Figure 5.3 shows significantly better constraints are obtained when using the  $C^{gg}$  data as a complement to the  $C^{tg}$  data, all the results show a good level of compatibility with Planck's results, with bands 3 and 4 and the combination of all bands clearly having a  $< 1\sigma$  compatibility.

We have also used the cross-correlation spectrum for our  $\Lambda$ CDM fiducial model with 10% errors as artificial data to analyse the constraint power that our idealized catalog would have on the  $\Omega_m$  parameter, the final result is shown in Figure 5.4, which does not showcase results much better than that of 2MASS' bands 3 and 4.

It is also important to highlight the work made in [81], in which the authors have analysed if changes in the data, including changes in the redshift distribution of the galaxies of the catalog used, would significantly improve the ISW signal. Despite exploring very different changes in the selection function compared to the ones made in this project, and other idealized properties for the data, it was also reported that the ISW signal would, even in an ideal scenario, still evade detection in  $> 10\%$  of cases.

In [22], the authors were able to find a signal-to-noise of  $4\sigma$  combining many surveys tracers of matter, the main ones being Planck's convergence lensing maps (Kappa) with a detection level of  $3.2\sigma$  and NVSS with  $2.6\sigma$ . These two datasets provide very deep data, with redshifts up to  $z = 5$ , and both have a good sky coverage, hinting that deeper surveys can yield better signals overall.

Ideally, detecting the ISW signal should consist of a combination of methods that are complementary, the angular cross-correlation studied here is a powerful one, but clearly has limitations. We have attempted to reduce the cosmic variance contribution to the errors with limited success, and comparing the results obtained here with other references, especially [22], leads us to think that, for an analysis using galaxy maps as tracers, the best current approach is to use deeper surveys such as NVSS.

# Appendices

# A | Demonstration of Accelerated Expansion Redshift

We will start defining the decelerating parameter  $q(a)$

$$q(a) \equiv -\frac{\ddot{a}a}{\dot{a}}. \quad (\text{A.1})$$

An expression for this parameter can be determined by dividing the second Friedmann equation (equation (2.9)) by the first Friedmann equation (equation (2.8)) and multiplying the result by minus one:

$$q(a) = -\frac{\ddot{a}a}{\dot{a}} = \frac{1}{2} \left( \frac{\rho + 3P}{\rho} \right). \quad (\text{A.2})$$

We will use  $\rho = \rho_m + \rho_{\text{de}} + \rho_r$  and assume  $\Omega_k = 0$ , meaning  $\rho = \rho_{\text{crit}}$ , so equation (A.2) becomes

$$q(a) = \frac{1}{2} \left( \frac{\rho_m + \rho_{\text{de}} + \rho_r + 3P}{\rho_{\text{crit}}} \right). \quad (\text{A.3})$$

As discussed in Section 2.1.3, it is commonly assumed that  $P_s = w_s \rho_s$ , so equation (A.3) becomes

$$q(a) = \frac{1}{2} \left[ \frac{\rho_m + \rho_{\text{de}} + \rho_r + 3(w_m \rho_m + w_r \rho_r + w_{\text{de}} \rho_{\text{de}})}{\rho_{\text{crit}}} \right]. \quad (\text{A.4})$$

We can use the values shown in Table 2.1 and use the definition of  $\Omega_s$  (equation (2.15)) to obtain

$$q(a) = \frac{1}{2} \Omega_m(a) + \Omega_r(a) + \frac{3w_{\text{de}} + 1}{2} \Omega_{\text{de}}(a) \quad (\text{A.5})$$

Using the evolution equations for  $\Omega_s(a)$  in terms of  $\Omega_s = \Omega_s(a_0)$  shown in [47]:

$$\Omega_m(a) = \frac{\Omega_m}{E(a)} a, \quad \Omega_r(a) = \frac{\Omega_r}{E(a)}, \quad \Omega_{\text{de}} = \frac{\Omega_{\text{de}}}{E(a)} a^{1-3w_{\text{de}}}, \quad (\text{A.6})$$

where  $E(a) = \Omega_r + \Omega_m a + \Omega_{\text{de}} a^{1-3w_{\text{de}}}$ , and taking  $\Omega_r = 0$ , we obtain

$$q(a) = \frac{1}{2} \left[ \frac{\Omega_m a + (1 + 3w_{\text{de}})\Omega_{\text{de}} a^{1-3w_{\text{de}}}}{\Omega_m a + \Omega_{\text{de}} a^{1-3w_{\text{de}}}} \right]. \quad (\text{A.7})$$

To find the scale factor in which the expansion's acceleration becomes positive, we can simply impose that  $q(a^*) = 0$ . Then we can change variables using  $a^* = 1/(1 + z^*)$  and solve for  $z^*$ , obtaining

$$z^* = \left[ -(1 + 3w_{\text{de}}) \frac{\Omega_{\text{de}}}{\Omega_m} \right]^{-\frac{1}{3w_{\text{de}}}} - 1 \quad (\text{A.8})$$

## B | Demonstration of Correlation Functions

Expanding the definition of  $C_\ell^{TT}$  given in (2.44) one can show that[33]:

$$C_\ell^{tt} = \frac{2}{\pi} \int dk k^2 P(k) \left| \frac{\Theta_\ell(k, \eta_0)}{\delta(k, \eta_0)} \right|^2. \quad (\text{B.1})$$

Similar expressions can be found for  $C_\ell^{tg}$  and  $C_\ell^{gg}$ , we will focus the demonstration on the temperature autocorrelation case.

Using the ISW term of equation (2.46)

$$\Theta_\ell^{\text{ISW}}(k, \eta_0) = \int_0^{\eta_0} d\eta e^{-\tau} [\Psi'(k, \eta) - \Phi'(k, \eta)] j_\ell[k(\eta_0 - \eta)], \quad (\text{B.2})$$

with  $e^{-\tau} \approx 1$  since, as shown, the ISW effect is only relevant at small scales<sup>1</sup>. So

$$\Theta_\ell^{\text{ISW}}(k, \eta_0) = \int_0^{\eta_0} d\eta \frac{d}{d\eta} [\Psi(k, \eta) - \Phi(k, \eta)] j_\ell[k(\eta_0 - \eta)], \quad (\text{B.3})$$

Using the definition of  $\eta$  in (2.47)

$$\eta = \int_0^t \frac{dt}{a(t)} = \int_0^a \frac{da'}{a'^2 H(a')} = \int_z^\infty \frac{dz'}{H(z)}, \quad (\text{B.4})$$

we can do a change in variables of the integral to redshift. Since

$$\eta_0 - \eta = \int_0^\infty \frac{dz'}{H(z')} - \int_z^\infty \frac{dz'}{H(z')} = \int_z^\infty \frac{dz'}{H(z')} = \chi(z), \quad (\text{B.5})$$

where  $\chi(z)$  is the comoving distance, equation (B.3) becomes

$$\Theta_\ell^{\text{ISW}}(k, z=0) = \int_0^\infty dz \frac{d}{dz} [\Psi(k, z) - \Phi(k, z)] j_\ell[k\chi(z)]. \quad (\text{B.6})$$

At late times, we can neglect anisotropic stress, taking  $\Psi \approx \Phi$ , therefore

$$\Theta_\ell^{\text{ISW}}(k, 0) = -2 \int_0^\infty dz \frac{d\Phi}{dz} j_\ell[k\chi(z)]. \quad (\text{B.7})$$

Finally, we can use the Poisson equation

---

<sup>1</sup>The Planck best-fit for the optical depth in the present is  $\tau = 0.054 \pm 0.007$

$$\Phi(k, z) = \frac{3}{2} \Omega_m \left( \frac{H_0}{k} \right)^2 (1+z) \delta(k, z), \quad (\text{B.8})$$

to show that

$$\delta(k, 0) = \frac{2}{3\Omega_m} \left( \frac{k}{H_0} \right)^2 \Phi(k, 0). \quad (\text{B.9})$$

With this:

$$\frac{\Theta_\ell(k, \eta_0)}{\delta(k, \eta_0)} = \frac{\Theta_\ell(k, z=0)}{\delta(k, z=0)} = -3\Omega_m \left( \frac{H_0}{k} \right)^2 \int_0^\infty dz \frac{d}{dz} \left[ \frac{\Phi(k, z)}{\Phi(k, 0)} \right] j_\ell[k\chi(z)]. \quad (\text{B.10})$$

Cosmologists define the growth function  $D(z)$  as

$$\frac{\Phi(k, a)}{\Phi(k, 1)} \equiv \frac{D(a)}{a} = (1+z)D(z) = \frac{\Phi(k, z)}{\Phi(k, 0)}, \quad (\text{B.11})$$

so

$$\frac{\Theta_\ell(k, \eta_0)}{\delta(k, \eta_0)} = -3\Omega_m \left( \frac{H_0}{k} \right)^2 \int_0^\infty \frac{d(1+z)D(z)}{dz} j_\ell[k\chi(z)]. \quad (\text{B.12})$$

Using this result, equation (B.1) in terms of redshift instead of  $\eta$  becomes

$$C_\ell^{tt} = \frac{2}{\pi} \int_0^\infty dk k^2 P(k) |W_\ell^t|^2 \quad (\text{B.13})$$

with

$$W_\ell^t = -3\Omega_m \left( \frac{H_0}{k} \right)^2 \int_0^\infty \frac{d(1+z)D(z)}{dz} j_\ell[k\chi(z)]. \quad (\text{B.14})$$

Equation (B.3) expresses the present contribution of the late ISW effect to the CMB temperature autocorrelation spectrum.

# Bibliography

- [1] A. A. Penzias and R. W. Wilson. “A Measurement of Excess Antenna Temperature at 4080 Mc/s.” In: *Astrophysical Journal* 142 (July 1965), pp. 419–421. DOI: 10.1086/148307.
- [2] Ivan Agullo, Dimitrios Kranas, and V Sreenath. “Large scale anomalies in the CMB and non-Gaussianity in bouncing cosmologies”. In: *Classical and Quantum Gravity* 38.6 (Feb. 2021), p. 065010. DOI: 10.1088/1361-6382/abc521. URL: <https://dx.doi.org/10.1088/1361-6382/abc521>.
- [3] Xingang Chen. “Primordial Non-Gaussianities from Inflation Models”. In: *Adv. Astron.* 2010 (2010), p. 638979. DOI: 10.1155/2010/638979. arXiv: 1002.1416 [astro-ph.CO].
- [4] Robert G. Crittenden and Neil Turok. “Looking for a Cosmological Constant with the Rees-Sciama Effect”. In: *Phys. Rev. Lett.* 76 (4 Jan. 1996), pp. 575–578. DOI: 10.1103/PhysRevLett.76.575. URL: <https://link.aps.org/doi/10.1103/PhysRevLett.76.575>.
- [5] G. Hinshaw et al. “FIVE-YEAR WILKINSON MICROWAVE ANISOTROPY PROBE\* OBSERVATIONS: DATA PROCESSING, SKY MAPS, AND BASIC RESULTS”. In: *The Astrophysical Journal Supplement Series* 180.2 (Feb. 2009), p. 225. DOI: 10.1088/0067-0049/180/2/225. URL: <https://dx.doi.org/10.1088/0067-0049/180/2/225>.
- [6] Planck Collaboration et al. “Planck 2018 results - VI. Cosmological parameters (Corrigendum)”. In: *Astronomy & Astrophysics* 652 (2021), p. C4. DOI: 10.1051/0004-6361/201833910e. URL: <https://doi.org/10.1051/0004-6361/201833910e>.
- [7] P. J. E. Peebles and J. T. Yu. “Primeval adiabatic perturbation in an expanding universe”. In: *Astrophys. J.* 162 (1970), pp. 815–836. DOI: 10.1086/150713.
- [8] D. J. Fixsen. “THE TEMPERATURE OF THE COSMIC MICROWAVE BACKGROUND”. In: *The Astrophysical Journal* 707.2 (Nov. 2009), p. 916. DOI: 10.1088/0004-637X/707/2/916. URL: <https://dx.doi.org/10.1088/0004-637X/707/2/916>.
- [9] Wayne Hu and Naoshi Sugiyama. “Anisotropies in the Cosmic Microwave Background: an Analytic Approach”. In: *The Astrophysical Journal* 444 (May 1995), p. 489. DOI: 10.1086/175624. arXiv: astro-ph/9407093 [astro-ph].
- [10] D. J. Fixsen et al. “Calibration of the COBE FIRAS Instrument”. In: *The Astrophysical Journal* 420 (Jan. 1994), p. 457. DOI: 10.1086/173577.
- [11] Marc Kamionkowski, Arthur Kosowsky, and Albert Stebbins. “A Probe of Primordial Gravity Waves and Vorticity”. In: *Phys. Rev. Lett.* 78 (11 Mar. 1997), pp. 2058–2061. DOI: 10.1103/PhysRevLett.78.2058. URL: <https://link.aps.org/doi/10.1103/PhysRevLett.78.2058>.

- [12] Silvia Galli et al. “CMB polarization can constrain cosmology better than CMB temperature”. In: *Phys. Rev. D* 90 (6 Sept. 2014), p. 063504. DOI: 10.1103/PhysRevD.90.063504. URL: <https://link.aps.org/doi/10.1103/PhysRevD.90.063504>.
- [13] P. A. R. Ade et al. “Improved Constraints on Primordial Gravitational Waves using Planck, WMAP, and BICEP/Keck Observations through the 2018 Observing Season”. In: *Phys. Rev. Lett.* 127 (15 Oct. 2021), p. 151301. DOI: 10.1103/PhysRevLett.127.151301. URL: <https://link.aps.org/doi/10.1103/PhysRevLett.127.151301>.
- [14] The Planck Collaboration. *The Scientific Programme of Planck*. 2006. arXiv: astro-ph/0604069 [astro-ph].
- [15] R. K. Sachs and A. M. Wolfe. “Perturbations of a cosmological model and angular variations of the microwave background”. In: *Astrophys. J.* 147 (1967), pp. 73–90. DOI: 10.1007/s10714-007-0448-9.
- [16] Robert G. Crittenden and Neil Turok. “Looking for a Cosmological Constant with the Rees-Sciama Effect”. In: *Phys. Rev. Lett.* 76 (4 Jan. 1996), pp. 575–578. DOI: 10.1103/PhysRevLett.76.575. URL: <https://link.aps.org/doi/10.1103/PhysRevLett.76.575>.
- [17] Asantha Cooray. “Integrated Sachs-Wolfe effect: Large scale structure correlation”. In: *Phys. Rev. D* 65 (10 Apr. 2002), p. 103510. DOI: 10.1103/PhysRevD.65.103510. URL: <https://link.aps.org/doi/10.1103/PhysRevD.65.103510>.
- [18] Stephen Boughn and Robert Crittenden. “A correlation between the cosmic microwave background and large-scale structure in the Universe”. In: *Nature* 427.6969 (Jan. 2004), pp. 45–47.
- [19] M. R. Nolta et al. “First Year Wilkinson Microwave Anisotropy Probe Observations: Dark Energy Induced Correlation with Radio Sources”. In: *The Astrophysical Journal* 608.1 (June 2004), p. 10. DOI: 10.1086/386536. URL: <https://dx.doi.org/10.1086/386536>.
- [20] Enrique Gaztañaga, Marc Manera, and Tuomas Multamäki. “New light on dark cosmos”. In: *Monthly Notices of the Royal Astronomical Society* 365.1 (Jan. 2006), pp. 171–177. ISSN: 0035-8711. DOI: 10.1111/j.1365-2966.2005.09680.x. eprint: <https://academic.oup.com/mnras/article-pdf/365/1/171/5534755/365-1-171.pdf>. URL: <https://doi.org/10.1111/j.1365-2966.2005.09680.x>.
- [21] Dupé, F.-X. et al. “Measuring the integrated Sachs-Wolfe effect”. In: *Astronomy and Astrophysics* 534 (Oct. 2011), A51. DOI: 10.1051/0004-6361/201015893. URL: <https://doi.org/10.1051/0004-6361/201015893>.
- [22] Planck Collaboration et al. “Planck 2015 results - XXI. The integrated Sachs-Wolfe effect”. In: *A&A* 594 (2016), A21. DOI: 10.1051/0004-6361/201525831. URL: <https://doi.org/10.1051/0004-6361/201525831>.
- [23] J. J. Condon et al. “The NRAO VLA Sky Survey”. In: *The Astronomical Journal* 115.5 (May 1998), p. 1693. DOI: 10.1086/300337. URL: <https://dx.doi.org/10.1086/300337>.

- [24] E. Moura-Santos et al. “A Bayesian Estimate of the CMB–large-scale Structure Cross-correlation”. In: *The Astrophysical Journal* 826.2 (July 2016), p. 121. DOI: 10.3847/0004-637X/826/2/121. URL: <https://dx.doi.org/10.3847/0004-637X/826/2/121>.
- [25] C. L. Bennett et al. “NINE-YEAR WILKINSON MICROWAVE ANISOTROPY PROBE (WMAP) OBSERVATIONS: FINAL MAPS AND RESULTS”. In: *The Astrophysical Journal Supplement Series* 208.2 (Sept. 2013), p. 20. DOI: 10.1088/0067-0049/208/2/20. URL: <https://dx.doi.org/10.1088/0067-0049/208/2/20>.
- [26] M. F. Skrutskie et al. “The Two Micron All Sky Survey (2MASS)”. In: *The Astronomical Journal* 131.2 (Feb. 2006), p. 1163. DOI: 10.1086/498708. URL: <https://dx.doi.org/10.1086/498708>.
- [27] Albert Einstein. “Cosmological Considerations in the General Theory of Relativity”. In: *Sitzungsber. Preuss. Akad. Wiss. Berlin (Math. Phys.)* 1917 (1917), pp. 142–152.
- [28] Y. Choquet-Bruhat. *General Relativity and the Einstein Equations*. Oxford Mathematical Monographs. OUP Oxford, 2008. ISBN: 9780191578854. URL: <https://books.google.com.br/books?id=UjHbm5rfpi8C>.
- [29] Suman Sarkar, Biswajit Pandey, and Rishi Khatri. “Testing isotropy in the Universe using photometric and spectroscopic data from the SDSS”. In: *Monthly Notices of the Royal Astronomical Society* 483.2 (Nov. 2018), pp. 2453–2464. ISSN: 0035-8711. DOI: 10.1093/mnras/sty3272. eprint: <https://academic.oup.com/mnras/article-pdf/483/2/2453/27184728/sty3272.pdf>. URL: <https://doi.org/10.1093/mnras/sty3272>.
- [30] Biswajit Pandey and Suman Sarkar. “Testing homogeneity of the galaxy distribution in the SDSS using Renyi entropy”. In: *Journal of Cosmology and Astroparticle Physics* 2021.07 (July 2021), p. 019. DOI: 10.1088/1475-7516/2021/07/019. URL: <https://dx.doi.org/10.1088/1475-7516/2021/07/019>.
- [31] Edwin Hubble. “A Relation between Distance and Radial Velocity among Extra-Galactic Nebulae”. In: *Proceedings of the National Academy of Science* 15.3 (Mar. 1929), pp. 168–173. DOI: 10.1073/pnas.15.3.168.
- [32] Georges Lemaitre. “A Homogeneous Universe of Constant Mass and Growing Radius Accounting for the Radial Velocity of Extragalactic Nebulae”. In: *Annales Soc. Sci. Bruxelles A* 47 (1927), pp. 49–59. DOI: 10.1007/s10714-013-1548-3.
- [33] S. Dodelson and F. Schmidt. *Modern Cosmology*. Elsevier Science, 2020. ISBN: 9780128159484. URL: <https://books.google.com.br/books?id=GGjfywEACAAJ>.
- [34] Fulvio Melia. “The Friedmann–Lemaître–Robertson–Walker metric”. In: *Modern Physics Letters A* 37.03 (2022), p. 2250016. DOI: 10.1142/S021773232250016X. eprint: <https://doi.org/10.1142/S021773232250016X>. URL: <https://doi.org/10.1142/S021773232250016X>.
- [35] Steven Weinberg. “The cosmological constant problem”. In: *Rev. Mod. Phys.* 61 (1 Jan. 1989), pp. 1–23. DOI: 10.1103/RevModPhys.61.1. URL: <https://link.aps.org/doi/10.1103/RevModPhys.61.1>.
- [36] Verónica Motta et al. “Taxonomy of Dark Energy Models”. In: *Universe* 7.6 (2021), p. 163. DOI: 10.3390/universe7060163. arXiv: 2104.04642 [astro-ph.CO].

- [37] B. Schutz. *A First Course in General Relativity*. Cambridge University Press, 2009. ISBN: 9780521887052.
- [38] Ofer Lahav and Andrew R Liddle. *The Cosmological Parameters 2014*. 2014. arXiv: 1401.1389 [astro-ph.CO].
- [39] Alan H. Guth. “Inflationary universe: A possible solution to the horizon and flatness problems”. In: *Phys. Rev. D* 23 (2 Jan. 1981), pp. 347–356. DOI: 10.1103/PhysRevD.23.347. URL: <https://link.aps.org/doi/10.1103/PhysRevD.23.347>.
- [40] A.D. Linde. “A new inflationary universe scenario: A possible solution of the horizon, flatness, homogeneity, isotropy and primordial monopole problems”. In: *Physics Letters B* 108.6 (1982), pp. 389–393. ISSN: 0370-2693. DOI: [https://doi.org/10.1016/0370-2693\(82\)91219-9](https://doi.org/10.1016/0370-2693(82)91219-9). URL: <https://www.sciencedirect.com/science/article/pii/0370269382912199>.
- [41] Antony Lewis, Anthony Challinor, and Anthony Lasenby. “Efficient computation of CMB anisotropies in closed FRW models”. In: *ApJ* 538 (2000), pp. 473–476. DOI: 10.1086/309179. arXiv: astro-ph/9911177 [astro-ph].
- [42] Antony Lewis and Sarah Bridle. “Cosmological parameters from CMB and other data: A Monte Carlo approach”. In: *PRD* 66 (2002), p. 103511. DOI: 10.1103/PhysRevD.66.103511. arXiv: astro-ph/0205436 [astro-ph].
- [43] D. J. Fixsen et al. “Calibration of the COBE FIRAS Instrument”. In: *The Astrophysical Journal* 420 (Jan. 1994), p. 457. DOI: 10.1086/173577.
- [44] Planck Collaboration et al. “Planck 2013 results. XXVII. Doppler boosting of the CMB: Eppur si muove”. In: *Astronomy & Astrophysics* 571 (2014), A27. DOI: 10.1051/0004-6361/201321556. URL: <https://doi.org/10.1051/0004-6361/201321556>.
- [45] Esteban Ricardo Chalbaud Mogollón. *Kinematic effects and the break of statistical isotropy of the cosmic microwave background fluctuations*. 2021. DOI: <https://doi.org/10.11606/D.43.2021.tde-31052021-162009>.
- [46] K. M. Górski et al. “HEALPix: A Framework for High-Resolution Discretization and Fast Analysis of Data Distributed on the Sphere”. In: *ApJ* 622 (Apr. 2005), pp. 759–771. DOI: 10.1086/427976. eprint: astro-ph/0409513.
- [47] José Carlos N. de Araujo. “The dark energy-dominated Universe”. In: *Astroparticle Physics* 23.2 (2005), pp. 279–286. ISSN: 0927-6505. DOI: <https://doi.org/10.1016/j.astropartphys.2004.12.004>. URL: <https://www.sciencedirect.com/science/article/pii/S0927650504002087>.
- [48] Robert G. Crittenden and Neil Turok. “Looking for a Cosmological Constant with the Rees-Sciama Effect”. In: *Phys. Rev. Lett.* 76 (4 Jan. 1996), pp. 575–578. DOI: 10.1103/PhysRevLett.76.575. URL: <https://link.aps.org/doi/10.1103/PhysRevLett.76.575>.
- [49] Niayesh Afshordi, Yeong-Shang Loh, and Michael A. Strauss. “Cross-correlation of the cosmic microwave background with the 2MASS galaxy survey: Signatures of dark energy, hot gas, and point sources”. In: *Phys. Rev. D* 69 (8 Apr. 2004), p. 083524. DOI: 10.1103/PhysRevD.69.083524. URL: <https://link.aps.org/doi/10.1103/PhysRevD.69.083524>.

- [50] S. P. Boughn and R. G. Crittenden. “The cross-correlation between the microwave and X-ray backgrounds: foregrounds and systematics”. In: *Monthly Notices of the Royal Astronomical Society* 360.3 (July 2005), pp. 1013–1021. ISSN: 0035-8711. DOI: 10.1111/j.1365-2966.2005.09090.x. eprint: <https://academic.oup.com/mnras/article-pdf/360/3/1013/3178164/360-3-1013.pdf>. URL: <https://doi.org/10.1111/j.1365-2966.2005.09090.x>.
- [51] S.P. Boughn and R.G. Crittenden. “A detection of the integrated Sachs–Wolfe effect”. In: *New Astronomy Reviews* 49.2 (2005). Sources and Detection of Dark Matter and Dark Energy in the Universe, pp. 75–78. ISSN: 1387-6473. DOI: <https://doi.org/10.1016/j.newar.2005.01.005>. URL: <https://www.sciencedirect.com/science/article/pii/S1387647305000096>.
- [52] A J Mead et al. “hmcode-2020: improved modelling of non-linear cosmological power spectra with baryonic feedback”. In: *Monthly Notices of the Royal Astronomical Society* 502.1 (Jan. 2021), pp. 1401–1422. ISSN: 0035-8711. DOI: 10.1093/mnras/stab082. eprint: <https://academic.oup.com/mnras/article-pdf/502/1/1401/42438464/stab082.pdf>. URL: <https://doi.org/10.1093/mnras/stab082>.
- [53] Eric V. Linder. “Exploring the Expansion History of the Universe”. In: *Phys. Rev. Lett.* 90 (9 Mar. 2003), p. 091301. DOI: 10.1103/PhysRevLett.90.091301. URL: <https://link.aps.org/doi/10.1103/PhysRevLett.90.091301>.
- [54] Chao-Jun Feng et al. “A new class of parametrization for dark energy without divergence”. In: *Journal of Cosmology and Astroparticle Physics* 2012.09 (Sept. 2012), p. 023. DOI: 10.1088/1475-7516/2012/09/023. URL: <https://dx.doi.org/10.1088/1475-7516/2012/09/023>.
- [55] A. Hernández-Almada et al. “Stability analysis and constraints on interacting viscous cosmology”. In: *Phys. Rev. D* 101 (6 Mar. 2020), p. 063516. DOI: 10.1103/PhysRevD.101.063516. URL: <https://link.aps.org/doi/10.1103/PhysRevD.101.063516>.
- [56] Ronaldo C. Batista. “A Short Review on Clustering Dark Energy”. In: *Universe* 8.1 (2022). ISSN: 2218-1997. DOI: 10.3390/universe8010022. URL: <https://www.mdpi.com/2218-1997/8/1/22>.
- [57] A. Amariti et al. “Brane cosmology and the self-tuning of the cosmological constant”. In: *Journal of Cosmology and Astroparticle Physics* 2019.10 (Oct. 2019), p. 007. DOI: 10.1088/1475-7516/2019/10/007. URL: <https://dx.doi.org/10.1088/1475-7516/2019/10/007>.
- [58] Mark S Linton et al. “Variable sound speed in interacting dark energy models”. In: *J. Cosmol. Astropart. Phys.* 2018.04 (Apr. 2018), pp. 043–043.
- [59] Marc Kamionkowski and Adam G. Riess. “The Hubble Tension and Early Dark Energy”. In: *Annual Review of Nuclear and Particle Science* 73.1 (2023), pp. 153–180. DOI: 10.1146/annurev-nucl-111422-024107. eprint: <https://doi.org/10.1146/annurev-nucl-111422-024107>. URL: <https://doi.org/10.1146/annurev-nucl-111422-024107>.

- [60] Planck Collaboration et al. “Planck 2018 results - V. CMB power spectra and likelihoods”. In: *Astronomy & Astrophysics* 641 (2020), A5. DOI: 10.1051/0004-6361/201936386. URL: <https://doi.org/10.1051/0004-6361/201936386>.
- [61] M. Betoule et al. “Improved cosmological constraints from a joint analysis of the SDSS-II and SNLS supernova samples”. In: *Astronomy & Astrophysics* 568, A22 (Aug. 2014), A22. DOI: 10.1051/0004-6361/201423413. arXiv: 1401.4064 [astro-ph.CO].
- [62] Julian E. Bautista et al. “Measurement of baryon acoustic oscillation correlations at  $z = 2.3$  with SDSS DR12 Ly $\alpha$ -Forests”. In: *Astronomy & Astrophysics* 603, A12 (June 2017), A12. DOI: 10.1051/0004-6361/201730533. arXiv: 1702.00176 [astro-ph.CO].
- [63] *GNU Scientific Library Reference Manual*. 3rd. GNU Project. URL: <http://www.gnu.org/software/gsl/>.
- [64] Eric Hivon et al. “MASTER of the Cosmic Microwave Background Anisotropy Power Spectrum: A Fast Method for Statistical Analysis of Large and Complex Cosmic Microwave Background Data Sets”. In: *The Astrophysical Journal* 567.1 (Mar. 2002), p. 2. DOI: 10.1086/338126. URL: <https://dx.doi.org/10.1086/338126>.
- [65] J. Jewell, S. Levin, and C. H. Anderson. “Application of Monte Carlo Algorithms to the Bayesian Analysis of the Cosmic Microwave Background”. In: *The Astrophysical Journal* 609.1 (July 2004), p. 1. DOI: 10.1086/383515. URL: <https://dx.doi.org/10.1086/383515>.
- [66] H. K. Eriksen et al. “Power Spectrum Estimation from High-Resolution Maps by Gibbs Sampling”. In: *The Astrophysical Journal Supplement Series* 155.2 (Dec. 2004), p. 227. DOI: 10.1086/425219. URL: <https://dx.doi.org/10.1086/425219>.
- [67] Benjamin D. Wandelt, David L. Larson, and Arun Lakshminarayanan. “Global, exact cosmic microwave background data analysis using Gibbs sampling”. In: *Phys. Rev. D* 70 (8 Oct. 2004), p. 083511. DOI: 10.1103/PhysRevD.70.083511. URL: <https://link.aps.org/doi/10.1103/PhysRevD.70.083511>.
- [68] M. Chu et al. “Cosmological parameter constraints as derived from the Wilkinson Microwave Anisotropy Probe data via Gibbs sampling and the Blackwell-Rao estimator”. In: *Phys. Rev. D* 71 (10 May 2005), p. 103002. DOI: 10.1103/PhysRevD.71.103002. URL: <https://link.aps.org/doi/10.1103/PhysRevD.71.103002>.
- [69] D. L. Larson et al. “Estimation of Polarized Power Spectra by Gibbs Sampling”. In: *The Astrophysical Journal* 656.2 (Feb. 2007), p. 653. DOI: 10.1086/509802. URL: <https://dx.doi.org/10.1086/509802>.
- [70] David J. Schlegel, Douglas P. Finkbeiner, and Marc Davis. “Maps of Dust Infrared Emission for Use in Estimation of Reddening and Cosmic Microwave Background Radiation Foregrounds”. In: *The Astrophysical Journal* 500.2 (June 1998), p. 525. DOI: 10.1086/305772. URL: <https://dx.doi.org/10.1086/305772>.
- [71] C. S. Kochanek et al. “The K-Band Galaxy Luminosity Function”. In: *The Astrophysical Journal* 560.2 (Oct. 2001), pp. 566–579. DOI: 10.1086/322488. arXiv: astro-ph/0011456 [astro-ph].

- [72] Maciej Bilicki et al. “Two Micron All Sky Survey Photometric Redshift Catalog: A Comprehensive Three-dimensional Census of the Whole Sky”. In: *The Astrophysical Journal Supplement Series* 210.1, 9 (Jan. 2014), p. 9. DOI: 10.1088/0067-0049/210/1/9. eprint: 1311.5246 (astro-ph.CO).
- [73] Edward L. Wright et al. “The Wide-field Infrared Survey Explorer (WISE): Mission Description and Initial On-orbit Performance”. In: *The Astronomical Journal* 140.6 (Dec. 2010), pp. 1868–1881. DOI: 10.1088/0004-6256/140/6/1868. arXiv: 1008.0031 [astro-ph.IM].
- [74] N. C. Hambly et al. “The SuperCOSMOS Sky Survey - I. Introduction and description”. In: *Monthly Notices of the Royal Astronomical Society* 326.4 (Oct. 2001), pp. 1279–1294. DOI: 10.1111/j.1365-2966.2001.04660.x. arXiv: astro-ph/0108286 [astro-ph].
- [75] M. R. Greason et al. *Wilkinson Microwave Anisotropy Probe (WMAP): Nine-Year Explanatory Supplement*. Available in electronic form at <http://lambda.gsfc.nasa.gov/>. NASA/GSFC. Greenbelt, MD, 2012.
- [76] Jesús Torrado and Antony Lewis. *Cobaya: Bayesian analysis in cosmology*. Astrophysics Source Code Library, record ascl:1910.019. Oct. 2019. ascl: 1910.019.
- [77] Jesús Torrado and Antony Lewis. “Cobaya: code for Bayesian analysis of hierarchical physical models”. In: *Journal of Cosmology and Astroparticle Physics* 2021.05 (May 2021), p. 057. DOI: 10.1088/1475-7516/2021/05/057. URL: <https://doi.org/10.1088%5C2F1475-7516%5C2F2021%5C%2F05%5C%2F057>.
- [78] Siddhartha Chib and Edward Greenberg. “Understanding the Metropolis-Hastings Algorithm”. In: *The American Statistician* 49.4 (1995), pp. 327–335. ISSN: 00031305. URL: <http://www.jstor.org/stable/2684568> (visited on 06/26/2024).
- [79] Andrew Gelman and Donald B. Rubin. “Inference from Iterative Simulation Using Multiple Sequences”. In: *Statistical Science* 7.4 (1992), pp. 457–472. DOI: 10.1214/ss/1177011136. URL: <https://doi.org/10.1214/ss/1177011136>.
- [80] R. C. Batista and F. Pace. “Structure formation in inhomogeneous Early Dark Energy models”. In: *JCAP* 06 (2013), p. 044. DOI: 10.1088/1475-7516/2013/06/044. arXiv: 1303.0414 [astro-ph.CO].
- [81] Caroline L. Francis and John A. Peacock. “Integrated Sachs–Wolfe measurements with photometric redshift surveys: 2MASS results and future prospects”. In: *Monthly Notices of the Royal Astronomical Society* 406.1 (July 2010), pp. 2–13. ISSN: 0035-8711. DOI: 10.1111/j.1365-2966.2010.16278.x. eprint: <https://academic.oup.com/mnras/article-pdf/406/1/2/3673745/mnras0406-0002.pdf>. URL: <https://doi.org/10.1111/j.1365-2966.2010.16278.x>.